Journal of Alloys and Compounds 947 (2023) 169448

Contents lists available at ScienceDirect

Journal of Alloys and Compounds

journal homepage: www.elsevier.com/locate/jalcom

Research Article

Activation of basal-plane sulfur sites on MoS_2 @Ni_3S_2 nanorods by Zr plasma ion implantation for bifunctional electrocatalysts

Ning Pang [a,1], Yun Li [c,1], Xin Tong [a,b,e], Mengqiu Wang [a], Huiyun Shi [a], Dajun Wu [b], Dayuan Xiong [a], Shaohui Xu [a], Lianwei Wang [a,e,*], Lin Jiang [d,**], Paul K. Chu [e]

[a] Key Laboratory of Polar Materials and Devices (MOE), Department of Electronics, East China Normal University, Shanghai 200241, China
[b] Jiangsu Laboratory of Advanced Functional Materials, School of Electronic and Information Engineering, Changshu Institute of Technology, Changshu 215500, China
[c] School of Physics and Electronic Engineering, Hanshan Normal University, Chaozhou 521041, China
[d] School of Microelectronics, Shanghai University, 20 Chengzhong Road, Shanghai 201800, China
[e] Department of Physics, Department of Materials Science and Engineering, and Department of Biomedical Engineering, City University of Hong Kong, Kowloon, Hong Kong, China

ARTICLE INFO

Article history:
Received 15 December 2022
Received in revised form 23 February 2023
Accepted 24 February 2023
Available online 2 March 2023

Keywords:
Zr plasma ion implantation
Heterogeneous nanorods
Interface modification
S empty state
Bifunctional electrocatalysts

ABSTRACT

Water electrolysis is one of the most promising technologies for sustainable and clean energy production, yet the sluggish kinetics of the hydrogen evolution reaction (HER) and oxygen evolution reaction (OER) hampers the commercialization. In this work, Zr-doped MoS_2 @Ni_3S_2 (MSNF) heterogeneous nanorods as bifunctional electrocatalysts were successfully explored to boost the catalytic activity of water electrolysis. The structural characterizations demonstrate the uniform modification of Zr atoms on the basal plane of MoS_2 at the heterointerface of MSNF. MSNF implanted with a Zr plasma ion fluence of 5×10^{16} ions-cm^{-2} (Zr500-MSNF) shows the most remarkable bifunctional electrocatalytic characteristics such as Tafel slope of 60.9 mV dec^{-1} and overpotential of 98 mV at 10 mA cm^{-2} for HER, as well as Tafel slope of 78.5 mV dec^{-1} and overpotential of 275 mV at 20 mA cm^{-2} for OER. Consistent with the structural and electrocatalytic characterizations, first-principles calculation confirms that the activated S sites in the basal plane of MoS_2 upon Zr doping have more empty states in its valence orbital to favor the adsorption of hydrogen and hydroxide, thus contributing to enhanced HER and OER activity. The findings in this work reveal a facile strategy to design high-performance and low-cost bifunctional catalysts based on two-dimensional materials for overall water splitting.

1. Introduction

The greenhouse effect and environmental contaminations caused by the assumption of fossil fuels pressingly demand the development of sustainable and clean energy [1]. Among the tremendous efforts devoted to reducing the carbon footprint [2], hydrogen energy has garnered the most attention owing to its zero-emission and high efficiency [3]. However, production of hydrogen by conventional techniques still requires fossil energy [4–6] and can hardly address the environmental concerns [7,8]. As a consequence, water splitting producing both hydrogen and oxygen via electrolysis appeals to be a promising option. Overall water splitting comprises two half reactions: the hydrogen evolution reaction (HER) and oxygen evolution reaction (OER) [9–11]. Currently, the commercialized HER and OER catalysts based on platinum and Ru/IrO_2 still suffer from high price and natural scarcity, thus largely limiting the large-scale production of hydrogen energy [12–14]. Therefore, the development of the low-cost and high-performance electrocatalysts to replace these noble metal ones is of high importance.

Transition metal compounds, especially the transition metal sulfides (TMSs), have aroused significant interests for water splitting electrocatalysis owing to the low price, environmental friendliness, and unique properties [15,16]. Predominant evidences have proved that the modulation of electronic configuration of TMSs via atomic modification and strain engineering can effectively enhance the

* Corresponding author at: Key Laboratory of Polar Materials and Devices (MOE), Department of Electronics, East China Normal University, Shanghai 200241, China.
** Corresponding author.
E-mail addresses: lwwang@ee.ecnu.edu.cn (L. Wang), linjiang@shu.edu.cn (L. Jiang).
[1] The authors contributed equally

https://doi.org/10.1016/j.jallcom.2023.169448
0925-8388/

electrocatalytic activity of HER and OER [17–20]. In particular, MoS_2 characterized with large surface area, good stability, and tunable electronic structure is appealing for water splitting electrocatalysis [21,22]. It has been demonstrated that the uncoordinated Mo-S sites at the edge is as active as Pt for HER [23]. However, the atom utilization efficiency is still limited with the dominant basal plane of MoS_2 being inactive [24]. Therefore, it is of great interest to activate the basal plane of MoS_2 for more efficient electrocatalysis of water splitting [25].

Constructing heterostructures [26] and atomic doping [27] are two main strategies to activate the MoS_2 basal plane. On one hand, the heterostructures can be prepared by incorporating MoS_2 with other materials to modulate the heteointerface of MoS_2 and thus the electronic configurations [28]. For example, MoS_2 nanoplates embedded in porous Co–N-doped carbon nanocages (MoS_2/Co–N–CN_2) exhibit improved activity (Tafel slope: the HER and OER values of 74 and 169 mV dec^{-1} respectively, overpotential: the HER and OER η10 values of 180 mV and 398 mV respectively) and stability in HER and OER owing to the modified electronic structure at the heterointerface favoring the adsorption of intermediates [29]. On the other hand, atomic doping via plasma ion implantation is compatible with high-efficient, low-temperature and large-scale operation for surface engineering of two-dimensional electrocatalysts [30]. In particular, Zr is an ideal dopant for regulating the electronic structure of transition metal compounds. Wei et al. reported Zr-doped transition metal phosphide on nitrogen-doped carbon fiber (P-CoFeZr/NCBC) as an efficient electrocatalyst of OER (Tafel slope: 51 mV/dec, overpotential: η10 values of 300 mV) due to the effectively modulated morphology and electronic structure by Zr [31]. Nevertheless, the electrocatalytic performance of the activated basal plane of MoS_2 still needs further improvement.

In this work, Zr-doped MoS_2 @Ni_3S_2 (MSNF) heteronanorods prepared by a one-step hydrothermal method and plasma ion implantation have been employed for efficient HER and OER electrocatalysis. The optimization of Zr ion fluences is closely related to the evolution of morphology, surface active area and electrocatalytic activity. Compared to other MSNF samples, the optimized Zr500-MSNF nanorods exhibit the lowest overpotentials (η_{20}) of 134 mV and 270 mV and Tafel slopes of 60.9 and 78.5 mV dec^{-1} in HER and OER, respectively. Structure characterizations demonstrate that more S sites in the basal plane of MoS_2 are activated by donating electrons to the doped Zr atom. First-principles calculation verifies that Zr produces more empty states at S sites in the basal plane to promote hydrogen adsorption in HER while Zr improves the adsorption and desorption of hydroxide at Ni sites in OER.

2. Experimental section

2.1. Chemicals

All the chemicals and the nickel foam (NF) were purchased from commercial vendors. The chemicals were used as received unless noted otherwise, and the nickel foam (NF) was used by cutting into pieces 2 cm × 3 cm in size. The solutions were prepared with 18 MΩ deionized (DI) water.

2.2. Synthesis of MoS_2@Ni_3S_2 nanorods

The NF substrate was washed with ethanol, diluted sulfuric acid (5 wt%), and DI water for 10 min to remove impurities. Na_2MoO_4 (0.3 mmol) and CH_4N_2S (12 mmol) were mixed in 50 mL of DI water and stirred for 20 min, yielding a transparent solution. The obtained solution and clean NF were transferred to an autoclave to anneal at a temperature of 200 °C for 12 h. After cooling to room temperature, the samples were taken out, and rinsed with absolute ethanol and DI water for 10 min to remove by-products, then the samples were dried in a vacuum oven at 80 °C for overnight, yielding the MoS_2 @ Ni_3S_2/NF.

2.3. Zr plasma implantation of MoS_2@Ni_3S_2 nanorods

Zr was implanted into MoS_2 @Ni_3S_2/NF (MSNF) with different fluences by using the high-energy metal plasma system in the Plasma Laboratory of City University of Hong Kong, and the scheme was shown in Fig. S1 [32]. The employed pressure was 2×10^{-3} Pa and the Zr target was ionized by an arc discharge to produce a Zr plasma which was accelerated to 25 kV and implanted into the sample that was grounded electrically. By adjusting the implantation time, different Zr fluences of 2.5×10^{16}, 5×10^{16}, and 10×10^{16} ions-cm^{-2} were implanted and the samples were designated as Zr250-MSNF, Zr500-MSNF, and Zr1000-MSNF, respectively.

2.4. Materials characterization

The morphology and elemental composition were characterized on a field-emission scanning electron microscope (FE-SEM, Zeiss Gemini 450, Germany) equipped with an energy dispersive X-ray spectrometer (EDS). The phase composition was analyzed by X-ray diffraction (XRD, Rigaku, RINT2100, Japan) with Cu K_α radiation (λ = 1.5406 Å). Transmission electron microscopy (TEM) and high-resolution TEM (HR-TEM) were conducted to examine the fine structure and lattice spacing on the JEOL JEM-2010. The elemental maps were obtained by EDS on the SEM and TEM and the concentrations were also determined by inductively-coupled plasma atomic emission spectroscopy (ICP-AES, Agilent, USA). The surface chemical states were analyzed by X-ray photoelectron spectroscopy (150 W, ESCALAB 250) with Al K_α radiation.

2.5. Electrochemical evaluation

The electrochemical analysis was performed using a three-electrode configuration on VMP3 (Bio-Logic) in 1 M KOH at room temperature [33]. The sample and saturated calomel electrode (SCE) were the working electrode and reference electrode, respectively. Graphite rods and platinum sheets were the counter electrodes in the HER and OER, respectively. The polarization curves for HER and OER were obtained by linear sweep voltammetry (LSV) at a scanning rate of 5 mV s^{-1} and the potential in the polarization curve was iR compensated by the ohmic resistance of the solution. The electrochemically active surface area (ECSA) was calculated by cyclic voltammetry (CV) carried out at different scanning rates in the non-faradaic potential region and the electric double layer capacitance (EDLC) was derived. Electrochemical impedance spectroscopy (EIS) was performed at the open circuit and related reaction potentials in the frequency range between 10^6 Hz and 10^{-1} Hz.

2.6. First-principles calculation

The first-principles calculation was conducted using the VASP code in which the generalized-gradient-approximation (GGA) [34] exchange-correlation functional [35] and projector augmented wave method was adopted [36]. The cutoff kinetic energy of the plane wave basis set was 450 eV. To evaluate the strong on-site Coulomb repulsion among electrons in the transition metal 3d or 4d orbitals, the GGA+*U* method [37] was implemented and (U-J) = 2.4 eV for the Mo and Zr 4d orbitals. The MoS_2 surface model in the supercell shown in Fig. S33 consisted of two (3 × 3)-unit-cell layers and a 13 Å thick vacuum layer. A Gamma-type 5 × 5 × 1 k-point mesh was applied to sample the Brillouin zone and all the atoms were fully relaxed until the forces on the atoms were less than 0.02 eV/Å. The Gibbs free energies on the Ni_3S_2 (110), MoS_2 (002), and Zr-MoS_2 (002) surfaces were derived for HER and OER.

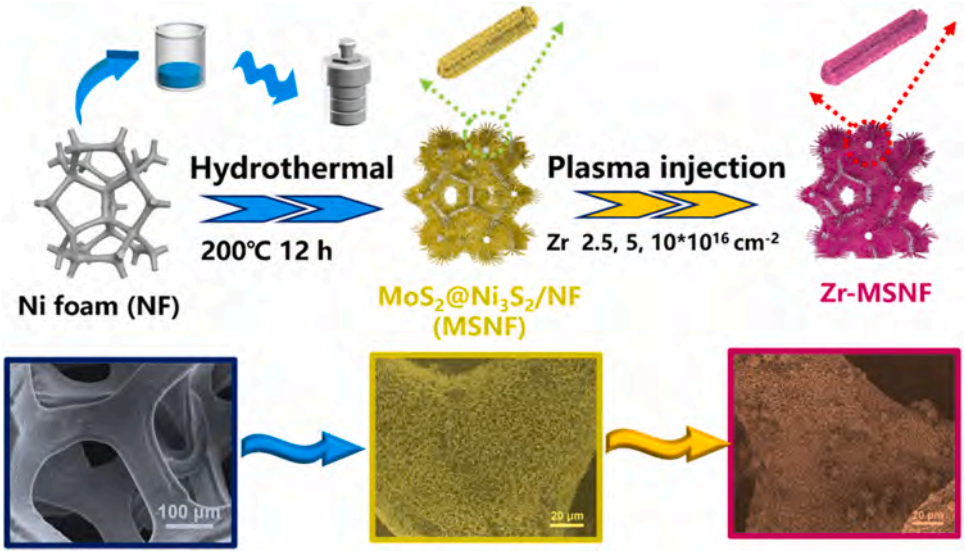

Fig. 1. Schematic diagram of the synthesis of Zr doped MoS_2 @Ni_3S_2/NF (Zr-MSNF) nanorods.

3. Results and discussion

3.1. Synthesis and Characterization of Zr-doped MoS_2@Ni_3S_2/NF nanorods

The Zr-doped MoS_2 @Ni_3S_2/NF nanorods were prepared following the steps showed in Fig. 1. In the first step, MoS_2 @Ni_3S_2/NF (MSNF) nanorods were synthesized by a one-step hydrothermal method as reported in the previous study [38] and Ni_3S_2/NF was also prepared for comparison. The mechanism of structure formation is as follows: firstly, nucleation on nickel foam is conducted through hydrothermal reaction, and then nanorods are formed through directional growth. During the growth of MoS_2 @Ni_3S_2, the filled nanorods may have a separation effect and form a unique rod-like structure [39,40]. With the obtained nanorods, the Zr with different fluences (2.5 ×10^{16}, 5 ×10^{16}, and 10 ×10^{16} ions-cm^{-2}) are plasma-implanted into the MSNF, and the samples are labeled Zr250-MSNF, Zr500-MSNF, and Zr1000-MSNF, respectively.

The phases of MSNF, Zr250-MSNF, Zr500-MSNF, and Zr1000-MSNF were determined by X-ray diffraction (XRD). As shown in Fig. 2a, all four samples exhibit sharp peaks at 45.3°, 52.4°, and 76.9° associated with the (111), (200), and (220) planes of the Ni substrate (PDF#04–0850) [41]. The diffraction peaks at 15.3°, 28.2°, 42.3°, 48.5°, 60.4°, and 72.4° marked by red pentagrams correspond to the (002), (004), (103), (105), (008), and (203) planes of MoS_2 (PDF#37–1492) [42] and the remaining diffraction peaks marked by blue squares are related to the (101), (110), (003), (211), and (300) planes of Ni_3S_2 (PDF#44–1418) [43]. With the increase of Zr ion fluences, the XRD peaks shift slightly to larger angles, which can be ascribed to the stress release rendered by the dopant.

The SEM-EDS spectra of Zr250-MSNF, Zr500-MSNF, and Zr1000-MSNF were shown in Fig. 2b, revealing the presence of Mo, S, Ni, and Zr. Figs. 2c and 2d depict the SEM images of the original Ni_3S_2 nanocones and bare MSNF nanorods, respectively. It is shown that the MSNF structure is slender and its length (8 μm) is larger than that of Ni_3S_2 nanocone structure (1 μm high). The ratio of Ni to S is 3:2 (Fig. S2) and Mo, Ni, and S are uniformly distributed in MSNF (Fig. S3), indicating the successful preparation of MSNF. As shown in Figs. 2e and 2f, the micro-morphology of Zr250-MSNF is basically unchanged compared to the pristine MSNF. When the Zr fluence is increased to 5×10^{16} ion-cm^{-2} (Zr500-MSNF), the MSNF nanorods collapse and partially agglomerate (Figs. 2g and 2h), suggesting the efficient doping of Zr into the MSNFs. After implantation with 10×10^{16} ion-cm^{-2} (Zr1000-MSNF), the original nanorods are fully intertwined to form a network and exhibit flower-liked shape (Figs. 2i and 2j). Uniform distributions of Mo, S, Ni, and Zr in Zr500-MSNF can be further confirmed from the EDS element maps in Fig. 2k, which is in line with the above SEM-EDS spectra.

To further investigate the influence of the Zr fluence on the microstructure, specific surface area is measured via the N_2 adsorption/desorption isotherms. The pore size distributions of Zr250-MSNF, Zr500-MSNF, and Zr1000-MSNF were characterized and compared (Figs. 3a and 3b). Meanwhile, the pore sizes for Ni_3S_2/NF and MSNF were also characterized and displayed in Fig. S4. The surface areas of Zr250-MSNF, Zr500-MSNF, and Zr1000-MSNF are approximately 33.2, 23.9, 16.2 m^2 g^{-1}, suggesting that a larger Zr fluence causes the vertical nanorods to collapse and leads to a smaller surface area. The corresponding pore diameters and pore volumes are 2.00, 2.00, 1.88 nm, and 0.027, 0.017, and 0.016 cm^3 g^{-1}, respectively, for Zr250-MSNF, Zr500-MSNF, and Zr1000-MSNF. The yielded results verify that the incorporation of Zr hardly change the size of the pores in the nanorods. Moreover, the Mo/Ni ratio of Zr-MSNF upon increasing Zr doping is steady to be around 3.8% (Fig. 3c) and the ratios of Zr to Mo (less than 8%) increase positively with ion fluences (Fig. 3c), indicating the stable atomic structure of MoS_2 upon Zr heteroatom doping.

The structure of Zr500-MSNF is further examined by TEM and HR-TEM. As shown in Figs. 3d and 3e, the length and width of the Zr500-MSNF nanorods are about 2 μm and 200 nm, respectively. Fig. 3e clearly showed the inner rod-like structure with Ni_3S_2 as the main body (left of the red box) and the surrounding structure of MoS_2 nanords (red box) and the MoS_2 nanosheets encapsulate the Ni_3S_2 nanorods, which is consistent with the observations from SEM images. The HR-TEM images of Zr500-MSNF NRs in Figs. 3f and 3g showed that there are two distinct lattice fringes with disclose lattice spacings of 0.60 and 0.31 nm, matching the (002) and (004) planes of MoS_2, and that of 0.28 nm is considered to originate from the (110) plane of Ni_3S_2, with yellow lines as the approximate interface in the middle. [44,45]. The selected-area electron diffraction (SAED) pattern (inset in Fig. 3g) shows the standard inverted grid arrangement of MoS_2. The TEM HAADF elemental maps in Fig. 3h illustrate uniform distributions of Mo, S, Ni, and Zr on the MSNF nanorods.

The chemical states of the pristine MSNF, Zr250-MSNF, Zr500-MSNF, and Zr1000-MSNF are characterized by X-ray photoelectron spectroscopy (XPS). The pristine Ni_3S_2/NF shows the presence of Ni,

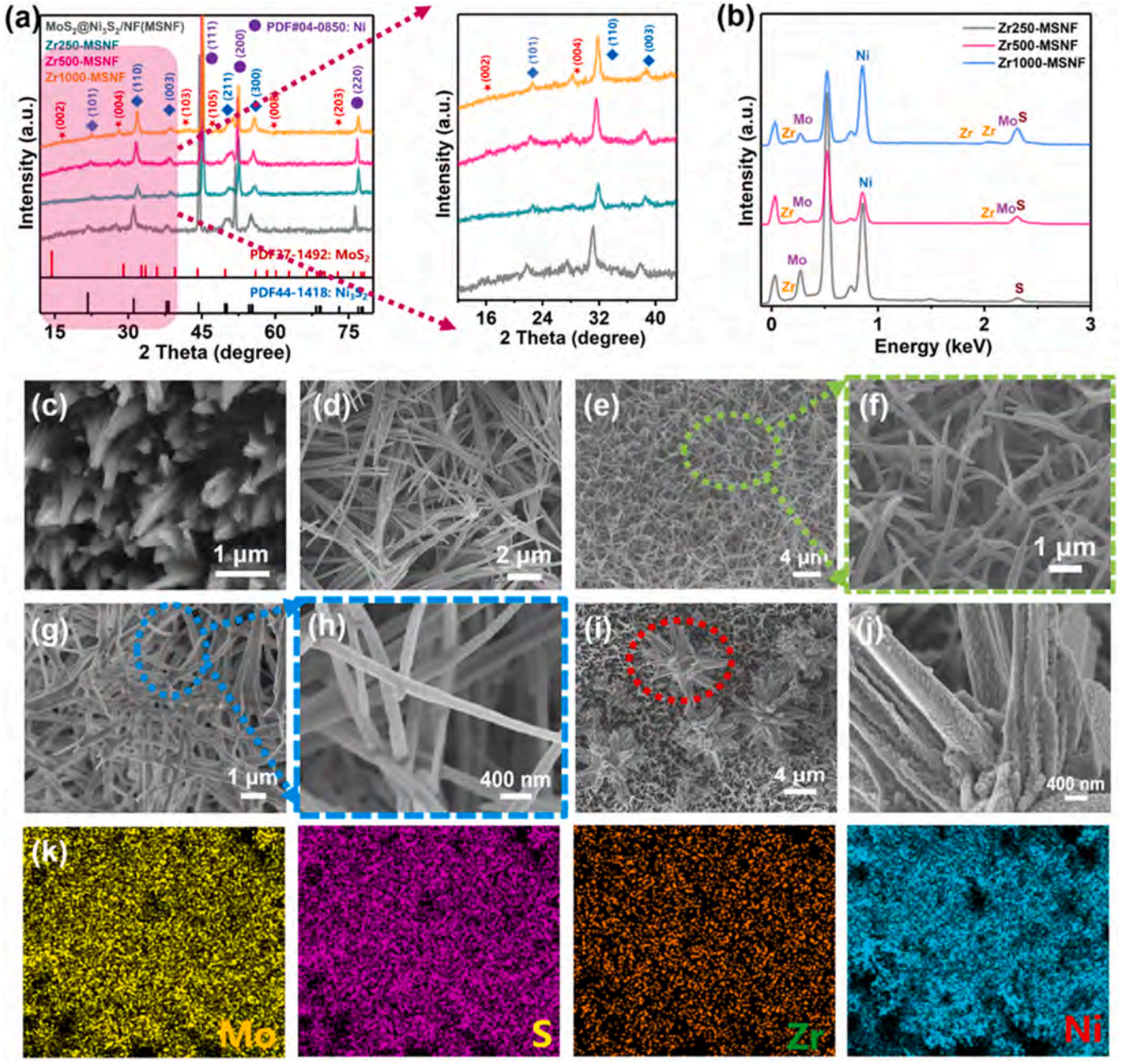

Fig. 2. (a) XRD patterns of MSNF, Zr250-MSNF, Zr500-MSNF, and Zr1000-MSNF; (b) EDS spectra of Zr250-MSNF, Zr500-MSNF, and Zr1000-MSNF; SEM images: (c) Ni_3S_2 nanocones, (d) MSNF nanorods, (e, f) Zr250-MSNF, (g, h) Zr500-MSNF, and (i, j) Zr1000-MSNF: (k) EDS elemental maps of Mo, S, Zr, and Ni in Zr500-MSNF.

S, and O, whereas MSNF shows the presence of Mo, S, Ni, and O. Mo, Ni, S, Zr, and O are detected from the Zr-doped MSNF samples, corroborating successful Zr plasma ion implantation (Fig. S5). The Mo 3d XPS spectrum of MSNF (Fig. 4a) exhibits two peaks at 228.7 and 231.8 eV corresponding to Mo $3d_{5/2}$ and Mo $3d_{3/2}$ [46]. With the increase of Zr fluence from 2.5×10^{16} to 1×10^{17} ions-cm^{-2}, the peaks of Mo $3d_{3/2}$ and Mo $3d_{5/2}$ in Fig. 4a shift slightly to a lower binding energy by 0.3 eV, implying that the outer layer of Mo receives electrons in the presence of Zr. The S $2p_{1/2}$ and S $2p_{3/2}$ peaks in Fig. 4b shift to high binding energy with the increase of Zr concentration, suggesting that the outer orbital of S loses electrons [47]. Similarly, the binding energies of Zr $3d_{3/2}$ and Zr $3d_{5/2}$ in Fig. 4c shift from 184.3 and 181.9 eV to 184.6 and 182.2 eV with the increase of Zr concentration, suggesting that Zr substitutes for Mo and the outer orbital of Zr also loses electrons [48]. The Ni 2p spectra in Fig. 4d show that the outer orbit of Ni gains electrons after plasma processing. Considering the electron loss of Zr and S, it can be concluded that electron flows from the outer orbitals of Zr and S to the outer orbitals of Mo and Ni after Zr plasma implantation, which is closely related with the HER and OER activity.

3.2. HER and OER properties

The HER activities of Pt/C, Ni_3S_2/NF, MSNF, Zr250-MSNF, Zr500-MSNF, and Zr1000-MSNF were measured in 1 M KOH at room temperature and the polarization curves are displayed in Fig. 5a after IR calibration. It is showed that Zr500-MSNF delivers excellent HER performance with a Tafel slope of 60.9 mV dec^{-1}, which is much less than that of the other electrodes (177.6 mV dec^{-1} for Ni_3S_2/NF, 144.7 mV dec^{-1} for MSNF, 115.3 mV dec^{-1} for Zr250-MSNF, and 88.7 mV dec^{-1} mV dec^{-1} for Zr1000-MSNF, Fig. 5b). The small Tafel

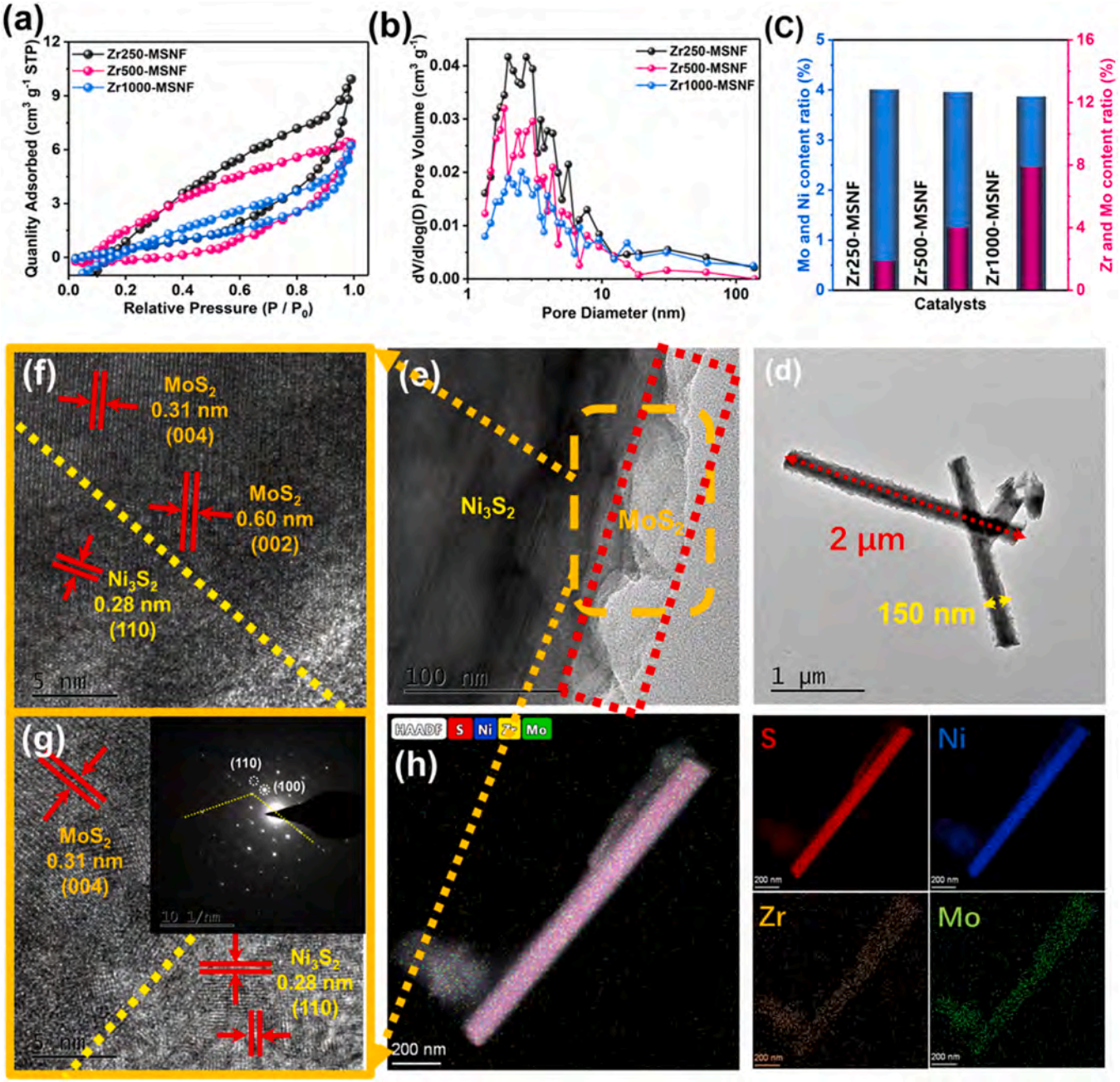

Fig. 3. (a) N_2 adsorption/desorption isotherms of Zr-doped MSNF; (b) Pore size distributions of Zr-doped MSNF. (c) Mo/Ni and Zr/Mo atomic ratios of Zr-doped MSNF determined by ICP; (d, e) TEM images of Zr500-MSNF nanorods; (f, g) HR-TEM images of Zr500-MSNF; (h) HAADF-TEM elemental maps of Zr500-MSNF.

slope of Zr500-MSNF implies that the HER process is likely to proceed by the Volmer-Heyrovsky mechanism [50].

The overpotentials comparison in Fig. 5c show that Zr500-MSNF needs overpotentials of 98 and 134 mV to drive current densities of 10 and 20 mA cm^{-2}, respectively, which are lower than those of Ni_3S_2/NF (321 and 362 mV), MSNF (293 and 331 mV), Zr250-MSNF (178 and 206 mV), and Zr1000-MSNF (149 and 185 mV). Such enhanced HER activity of Zr-doped MSNF is considered to be closely related to the electron redistributions as described above. Specifically, such redistribution between Zr, Mo and S create more empty states in the valence orbital of MoS_2, thus favoring the adsorption of H^+ and HER activity. With the increase of the Zr fluence from 0 to 1×10^{17} ions-cm^{-2}, the HER catalytic activity of MSNF firstly increases sharply (Zr250-MSNF and Zr500-MSNF) and then declines slowly (Zr1000-MSNF). When the Zr fluence is 5×10^{16} ions-cm^{-2}, The Zr500-MSNF doped with a Zr fluence is 5×10^{16} ions-cm^{-2} exhibits superior HER performance over others (inset in Fig. 5c). The slow decline with higher Zr doping level may be caused by the collapse of nanorods, which results in a smaller surface area.

Moreover, electrochemical impedance spectroscopy (EIS) is carried out at − 0.1 V vs. RHE to study the ion resistance and charge transfer resistance, which are considered as the vital indicators to evaluate the HER properties (Fig. 5d) [49]. The obtained results revealed that the resistance of the solution R_s is relatively stable at 1 ~ 1.3 Ω after Zr plasma ion implantation. The charge transfer resistance (R_{ct}) of Zr500-MSNF is approx 5.1 Ω, which is smaller than those of MSNF (19.8 Ω), Zr250-MSNF (8.3 Ω), and Zr1000-MSNF (6.5 Ω). These differences indicate that Zr500-MSNF holds the fastest electron transport among these nanorods, and the involved catalytic reaction is faster in the electric double layer between the electrode

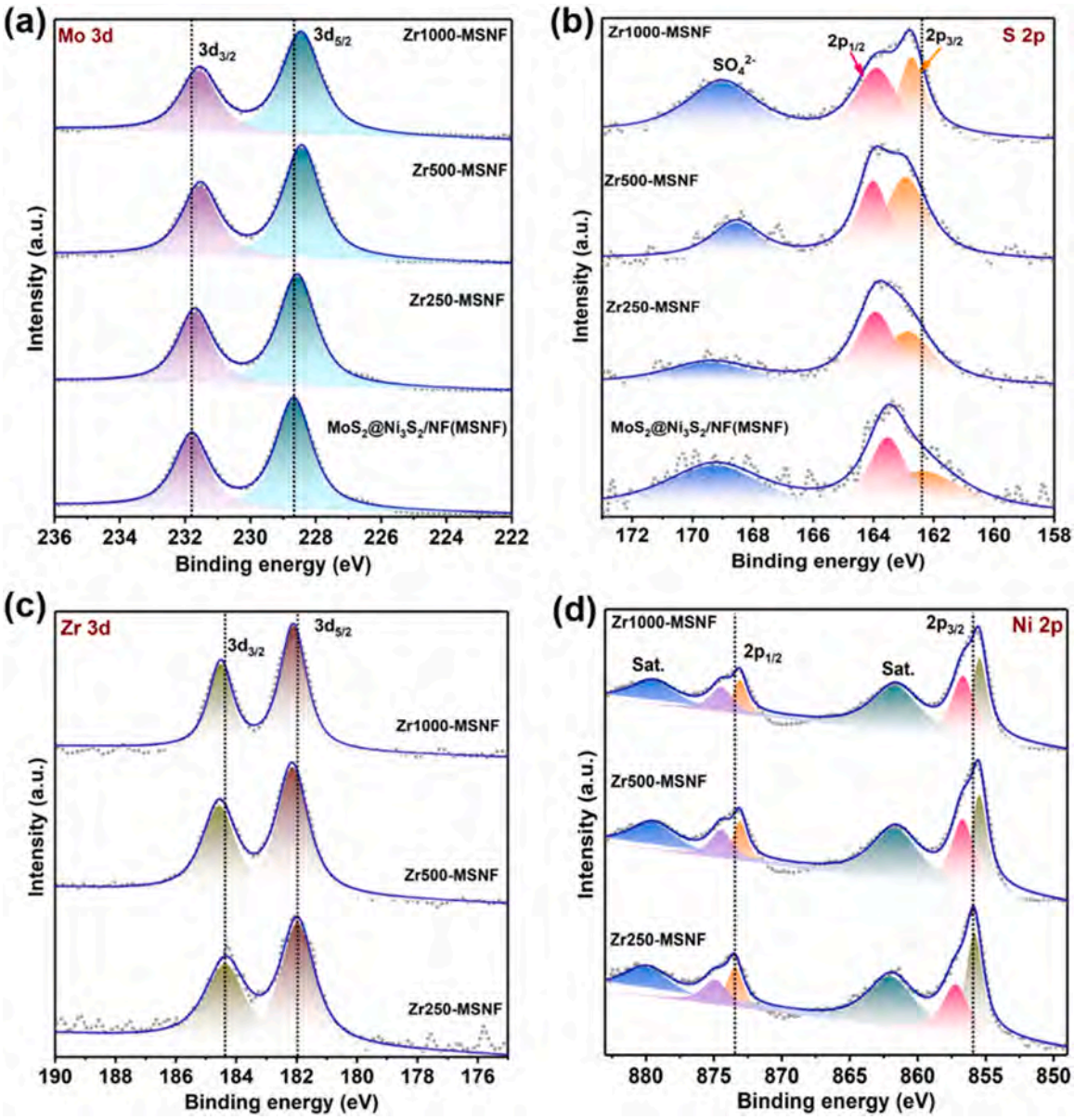

Fig. 4. High-resolution XPS spectra: (a) Mo 3d, (b) S 2p, (c) Zr 3d, and (d) Ni 2p.

surface and electrolyte, which are consistent with the data obtained from LSV curves. The electrochemical double layer capacitance (EDLC) obtained by CV in the non-Faraday region is another important parameter to determine the electrochemical surface area (ECSA). It is deemed that the larger the EDLC, the larger is ECSA of the electrode. The EDLC of Zr500-MSNF electrode (Fig. S6) shows a value of 26.8 mF cm^{-2}, which is bigger than those of Ni_3S_2/NF (7.3 mF cm^{-2}), MSNF (9.1 mF cm^{-2}), Zr250-MSNF (11.2 mF cm^{-2}), and Zr1000-MSNF (16.1 mF cm^{-2}). Obviously, Zr500-MSNF holds a larger electrochemically active area and more active sites, which is benefitial for the hydrogen evolution. Further studies indicated that Zr-doping effectively enhances the catalytic stability of MSNF electrodes. As shown in Figs. 5f, 88.9% of the HER current density of Zr500-MSNF is maintained after operation for 30 h in the alkaline solution.

The LSV curves of OER obtained from RuO_2, Ni_3S_2/NF, MSNF, Zr250-MSNF, Zr500-MSNF, and Zr1000-MSNF were shown in Fig. 6a. In addition to the current increase due to oxygen evolution process, a peak at 1.62 V vs. RHE for Ni_3S_2/NF is observed and can be ascribed to the typical oxidation peak of Ni^{2+} to Ni^{3+}. Such oxidation peak that can interfere with OER activity is hardly observed in MSNF samples due to the covering of MoS_2 nanosheets at the outer-surface of Ni_3S_2/NF. Hence, MSNF, Zr250-MSNF, Zr500-MSNF, and Zr1000-MSNF shows more excellent OER performance than Ni_3S_2/NF. The overpotentials to yield current densities of 20 and 50 mA cm^{-2} (η_{20} and η_{50}) are shown in Fig. 6b. It is revealed that η_{20} and η_{50} of Zr500-MSNF are 275 and 298 mV, which are less than those of Ni_3S_2/NF (523 and 602 mV), MSNF (346 and 404 mV), Zr250-MSNF (297 and 334 mV), and Zr1000-MSNF (316 and 351 mV). Furthermore, Zr500-MSNF shows a Tafel slope of 78.5 mV dec^{-1}, which is smaller than those of Ni_3S_2/NF (166.4 mV dec^{-1}), MSNF (133.8 mV dec^{-1}), Zr250-MSNF (113.7 mV dec^{-1}), and Zr1000-MSNF (96.8, mV dec^{-1}), reflecting faster reaction kinetics and higher OER activity (Fig. 6c). Considering the absence of oxidation peak of Ni^{2+} to Ni^{3+}in MSNF samples, it is assumed that origin of the activity enhancement at Zr-doped MSNF is the MoS2 outer layer doped with Zr heteroatoms.

In general, the large electrochemically active surface area (ECSA) is benefit to the OER electrocatalytic activity [51], whereas the ECSA is proportional to the double-layer capacitance (C_{dl}). Herein C_{dl} is calculated based on the CV curves acquired at different scanning

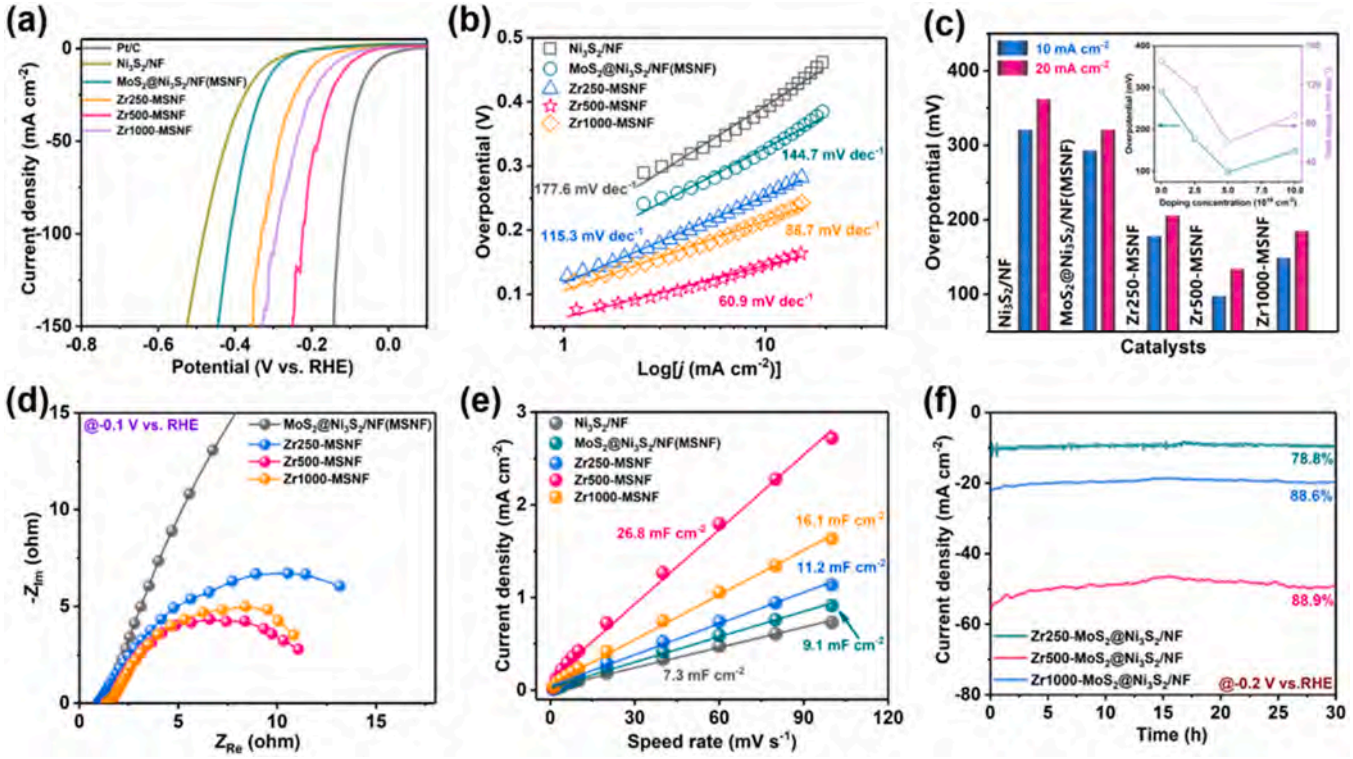

Fig. 5. Electrocatalytic HER characteristics: (a) Polarization curves, (b) Tafel plots, (c) Overpotentials, (d) EIS Nyquist plots at − 0.1 V vs. RHE, (e) EDLCs, and (f) Stability evaluation.

rates in the non-Faraday region and is shown in Fig. 6d. It is observed that Zr500-MSNF has the largest C_{dl} of 44.3 mF cm^{-2}, which is almost 4 times that of Ni_3S_2/NF (10.5 mF cm^{-2}) and MSNF (15.2 mF cm^{-2}), and is larger than those of Zr250-MSNF (30.1 mF cm^{-2}) and Zr1000-MSNF (33.4 mF cm^{-2}). Such a high C_{dl} value can be ascribed to the large electrochemical active areas and the presence of more active sites in Zr500-MSNF, which is consistent with the boosted OER activity as shown in Fig. 6b-c. Moreover, Zr500-MSNF shows a similar solution resistance at the open circuit potential and the slope of the electron transfer resistance Zr500-MSNF is the largest (Fig. 6e), suggesting that electron transfer is the fastest and the reaction rate is also the fastest. Moreover, the long-term stability for

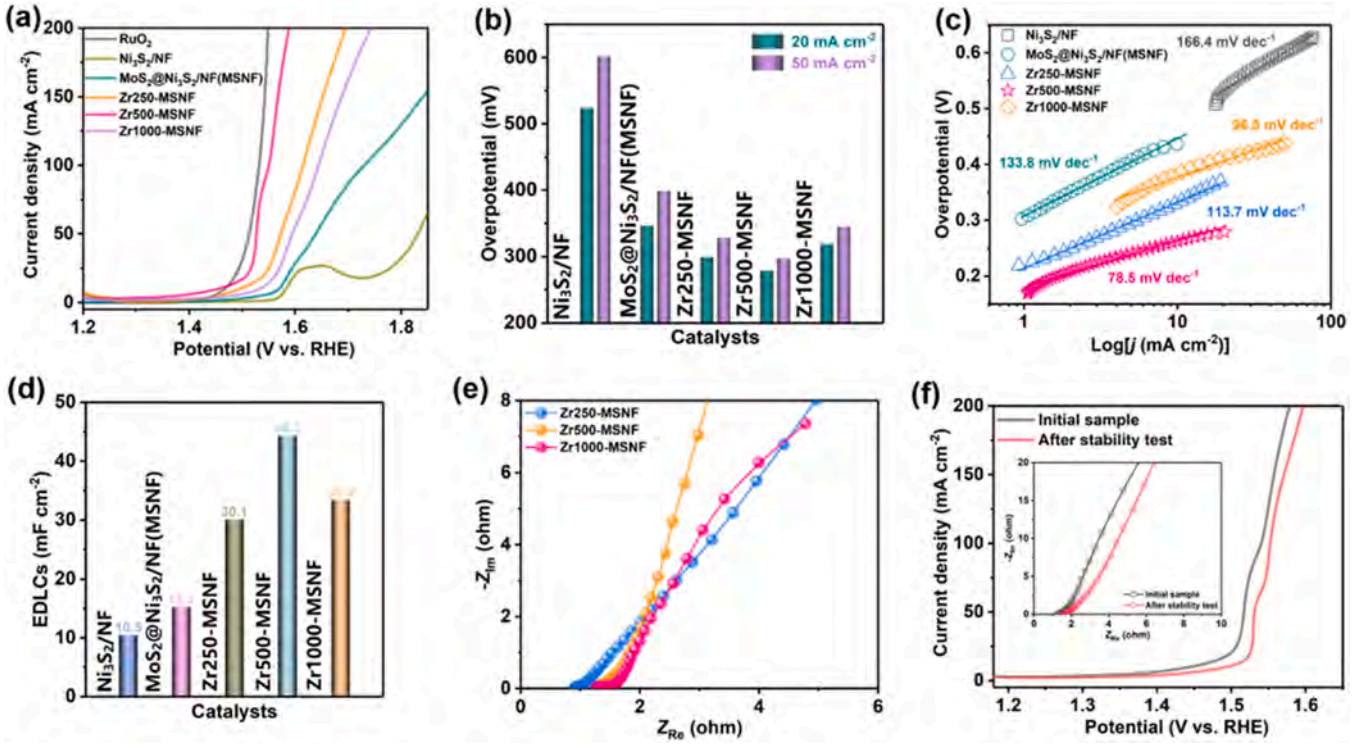

Fig. 6. Electrocatalytic OER characteristics: (a) Polarization curves, (b) Overpotentials, (c) Tafel plots, (d) EDLCs, (e) EIS Nyquist plots at OCV, and (f) Stability assessment.

OER is characterized and shown in Fig. 6f. The polarization curve of Zr500-MSNF after the long-term stability test is only slightly attenuated compared to the original electrode. The impedance shifts to the right because the Zr500-MSNF nanorods collapse slightly during the test and electron transfer slows (inset in Fig. 6f). With LSV, EDLC, EIS and other data, it is verified that Zr ion implantation in MSNF heterojunction successfully acts as an excellent bifunctional catalyst. Especially, MoS_2 covering the underlying Ni_3S_2 nanostructure avoids the influence of metal ion oxidation peak, forming a stable OER electrode.

3.3. Analysis of HER and OER enhancement mechanism

First-principles calculation is performed to investigate the activation effects of Zr doping on the catalytic activity of MoS_2 for overall water splitting. The relevant reactions and calculation details are provided in Supplementary Materials. The hydrogen adsorption energy is an important parameter to evaluate the catalytic activity of the electrode in HER and the closer it is to zero, the higher is the catalytic activity. Herein, hydrogen adsorption on the MoS_2 (002), Ni_3S_2 (110), Zr-doped MoS_2 (002), and Zr-doped Ni_3S_2 (110) surfaces is considered. According to the experimental results, the models are presented in Fig. 7a and Fig. S7-9. The Gibbs free energies of S sites at different positions in the basal plane of Zr-doped MoS_2 with different dopant concentrations are derived. the Gibbs free energies of S sites in the pristine MoS_2 and Ni_3S_2 basal planes are high implying weak HER activity. Zr doping enhances hydrogen adsorption on the S site in the MoS_2 basal plane and the adsorption free energy of H^* (ΔG_{H^*}) decreases from 1.88 to 0.44 eV (Fig. 7b). Furthermore, The Gibbs free energy of the S site directly in contact with Zr is approximately 0.4 eV and 0.2 eV smaller than that of other S sites, implying that the S site in direct contact with Zr is the active HER site and has higher catalytic activity (Fig. 7c). As the concentration of Zr goes up from 11% to 33%, the adsorption energies of H^* on the directly connected S sites are close. When the dopant concentration increases by a factor of two, the directly connected active S sites also increase by a factor of two consistent with the experimental results.

The density of states (DOS) [66] in Fig. 7d reveals the effects of impurity atoms on valence electrons. The valence band of pure MoS_2 is full, Mo can get 4 electrons from its surroundings, and the S site

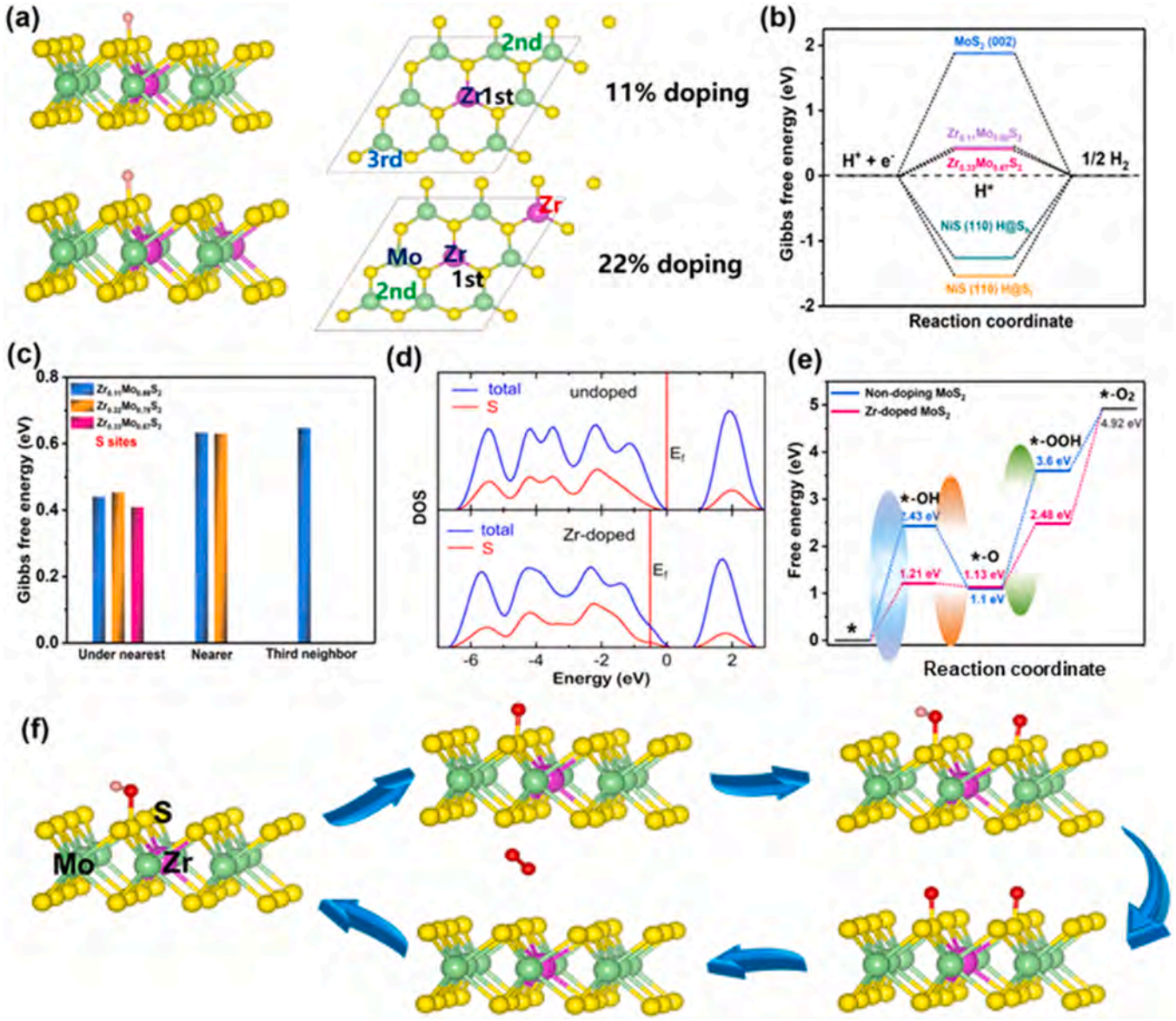

Fig. 7. (a) Optimized structure for H^* adsorption on Zr-MoS_2 (002); (b) ΔG_{H^*} for HER; (c) ΔG_{H^*} of H^* adsorbed on S sites at different neighbors; (d) DOS of S sites on MoS_2 and Zr-MoS_2; (e) Free energy diagram on S sites in OER; (f) Schematic illustration of OH^* /O^* /OOH^* /OO^* generation and oxygen formation on S sites of Zr-MoS_2 in 1.0 M KOH.

next to it adsorbs 4 vacancies to Mo site, making the valence orbital of S saturated and the valence orbital of S is saturated. Therefore, it is difficult for H* to adsorb onto the S site resulting in a larger ΔG_{H^*}. Incorporation of dopants with fewer valence electrons than Mo causes vacancies to emerge from the valence band, and the smaller the number of valence electrons, the larger is the number of vacancies. The DOS of directly connected S atoms in Zr plasma-treated MoS_2 is displayed in Fig. 7d Zr has fewer unsaturated electrons and can only provide 2–3 vacancies. The valence orbitals and empty states in the valence orbitals of S atoms also increase, resulting in enhanced activity of S sites. Therefore, it is relatively easy for H* to adsorb onto the active site of S and ΔG_{H^*} is closer to zero thereby favorable to H* adsorption and desorption. The results suggest that incorporation of Zr optimizes ΔG_{H^*} in HER on S sites in the MoS_2 basal plane.

In the same way, the origin of the enhanced OER activity of MoS_2 @Ni_3S_2 by plasmonic doping of Zr can be explained by first-principles calculation. Specifically, we evaluate and compare the Gibbs free energies of the oxygen-containing intermediate states of OH* , O* , OOH* , and OO* on the S sites in the pristine MoS_2 (002), Ni_3S_2 (110) and Zr doped MoS_2 (002) basal plane. As shown in Fig. S10, the S site in nickel sulfide is oxidized and converted to sulfate in the solution after adsorbing OH* , while nickel sulfide is converted to NiOOH. This explains why Ni_3S_2 shows an obvious Ni^{2+} to Ni^{3+} transformation during oxygen evolution and produces an oxidation peak. The Gibbs free energies of the corresponding converted $Ni(OH)_2$ for the adsorption of intermediates during oxygen evolution are shown in Fig. S11. On the contrary, the adsorption process of the oxygen-containing intermediate state at the S site in the MoS_2 basal plane is stable and the oxygen evolution reaction occurs mainly on the surface of MoS_2 (Fig. S12). Fig. 7f shows the adsorption process of the oxygen-containing intermediate states OH* , O* , OOH* , and OO* on the Zr plasma-doped MoS_2 (002) surface and it includes all the steps in the oxygen evolution reaction. Since OH* , O* and OOH* are the key intermediates in OER, the Gibbs free energies of undoped MoS_2 and Zr-doped MoS_2 are compared with these two adsorbed intermediates and it is found that the Gibbs free energies of Zr-doped MoS_2 (1.21, −0.08 and 1.35 eV) in these steps are smaller than those of undoped MoS_2 (2.43, −1.3 and 2.5 eV) and $Ni(OH)_2$, explaining the better oxygen evolution activity (Fig. 7e). As a consequence, unsaturation of S-site atomic orbitals in the MoS_2 basal plane and generation of empty states created by Zr plasma implantation enhance the OER activity.

3.4. Overall water splitting

To investigate the practicality in overall water splitting, Zr500-MSNF was employed as both the anode and cathode in an alkaline medium (Fig. 8a). The two-electrode overall water splitting system was constructed and depicted in Fig. S13. The polarization curves acquired from Ni_3S_2/NF // Ni_3S_2/NF, MSNF // MSNF, and Zr500-MSNF // Zr500-MSNF in overall water splitting were shown in Fig. 8b. It's obvious that Zr500-MSNF // Zr500-MSNF needs a small cell voltage of 1.49 V to drive a current density of 10 mA cm^{-2}, which is far superior to Ni_3S_2/NF // Ni_3S_2/NF (1.56 V) and MSNF // MSNF (1.78 V). This is considered to be associated to the better catalytic activity of Zr500-MSNF in both HER and OER. Furthermore, Faraday efficiency (FE) was further studied to investigate the relationship between the actual produced H_2 / O_2 and the theoretical production value. As shown in Fig. 8c, the Zr500-MSNF electrode achieves stable hydrogen/oxygen yields, and its Faradaic efficiencies for HER and OER are close to 100%, indicating that the actual yields agree well with the theoretical values. Furthermore, the activity of Zr500-MSNF // Zr500-MSNF decline and maintains at 92.9% after operation for 50 h at 1.6 V, which is better than the other two electrodes (Ni_3S_2/NF // Ni_3S_2/NF (77.4%), MSNF // MSNF (84.8%), Fig. 8d). The TEM image of Zr500-MSNF after the stability test discloses a relatively intact nanorod morphology and clear interplanar spacing of MoS_2 (002) (Fig.

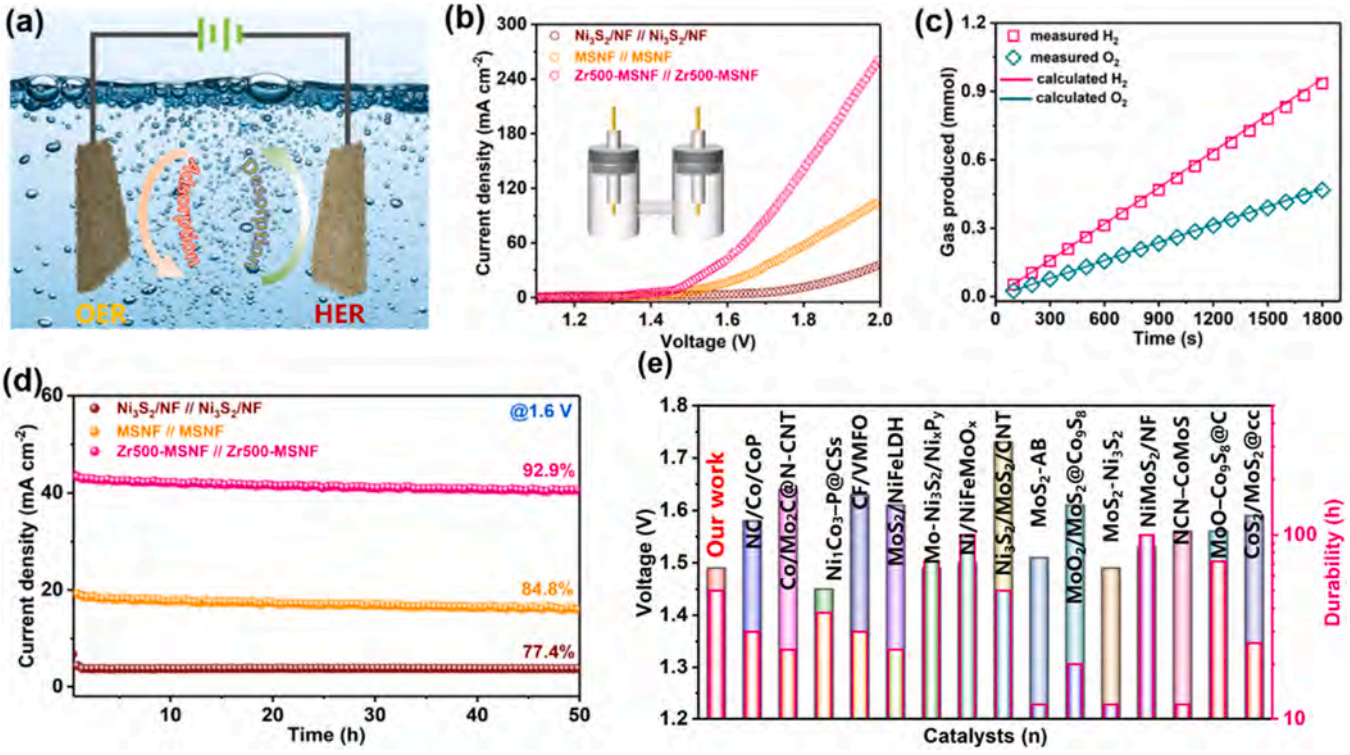

Fig. 8. (a) Schematic diagram of the two-electrode water electrolysis system; (b) Polarization curves of two-electrode overall water splitting; (c) Comparison of the experimental and theoretical amount of H_2 and O_2 produced in overall water splitting; (d) Galvanostatic measurement performed at a cell voltage of 1.6 V in 1.0 M KOH; (e) Comparison of the overall water splitting properties between Zr500-MSNF and electrocatalysts in the recent literature.

S14), indicating the good stability of Zr500-MSNF electrode. The obtained results showed that Zr500-MSNF exhibits outstanding catalytic activity in respect to previous reports. [50–65].

4. Conclusion

In this manuscript, we report the modification of MSNF nanorods via using systematic Zr plasma ion implantation, and their enhanced bifunctional catalytic properties in alkaline HER and OER. It is shown that the catalytic activity of Zr-doped MSNFs for both HER and OER increase sharply with the addition of Zr ion fluence, and then decreases slowly when Zr ion fluence reaching 5×10^{16} ions-cm^{-2}. Zr500-MSNF shows the best bifunctional electrochemical performance as proved by the Tafel slope (the HER and OER values of 60.9 and 78.5 mV dec^{-1} respectively), overpotential (the HER and OER η20 values of 134 mV and 270 mV respectively), and long-term durability (maintains at 92.9% after operation for 50 h at 1.6 V). Experimental and theoretical evaluation showed that Zr doping at the MSNF interface replaced Mo and induced electron loss at the basal plane S sites of MoS_2, thus activating the S sites with more empty states in the valence orbital for promoted HER and OER. This work reveals a facile and scalable strategy for modulating the atomic and electronic structure of two-dimensional materials and provide insights into the development of high-performance bifunctional water splitting catalysts.

CRediT authorship contribution statement

Ning Pang: Investigation, Data curation, Form alanalys, Writing – original draft. **Yun Li:** Conceptualization, Writing – review & editing, Funding acquisition. **Xin Tong:** Formal analysis. **Mengqiu Wang:** Resources. **Huiyun Shi:** Investigation. **Dajun Wu:** Supervision, Formal analysis. **Dayuan Xiong:** Discussion, Funding acquisition. **Shaohui Xu:** Project administration. **Lianwei Wang:** Discussion, Validation, Resources. **Lin Jiang:** Discussion, Methodology, Writing – review & editing. **Paul K. Chu:** Funding acquisition, Writing – review & editing.

Data Availability

Data will be made available on request.

Declaration of Competing Interest

The authors declare that they have no known competing financial interests or personal relationships that could have appeared to influence the work reported in this paper.

Acknowledgements

This work was jointly supported by National Natural Science Foundation of China under Grant No. 61991444, Science and Technology Commission of Shanghai Municipality (Grant No. 18DZ2270800) and City University of Hong Kong Strategic Research Grant (SRG) (No. 7005105). Yun Li thanks the support of the Scientific Research Foundation for the Returned Overseas Chinese Scholars of State Education Ministry (Grant No. [2015]−1098).

Appendix A. Supporting information

Supplementary data associated with this article can be found in the online version at doi:10.1016/j.jallcom.2023.169448.

References

[1] S. Zhao, C. Tan, C.-T. He, P. An, F. Xie, S. Jiang, Y. Zhu, K.-H. Wu, B. Zhang, H. Li, J. Zhang, Y. Chen, S. Liu, J. Dong, Z. Tang, Structural transformation of highly active metal-organic framework electrocatalysts during the oxygen evolution reaction, Nat. Energy 5 (2020) 881–890.
[2] J. Kang, X. Qiu, Q. Hu, J. Zhong, X. Gao, R. Huang, C. Wan, L. Liu, X. Duan, L. Kang, Valence oscillation and dynamic active sites in monolayer NiCo hydroxides for water oxidation, Nat. Catal. 4 (2021) 1050–1058.
[3] B. Zhang, S. Yu, Y. Dai, X. Huang, L. Chou, G. Lu, G. Dong, Y. Bi, Nitrogen-incorporation activates $NiFeO_x$ catalysts for efficiently boosting oxygen evolution activity and stability of $BiVO_4$ photoanodes, Nat. Commun. 12 (2021) 6969.
[4] C. Lin, J. Li, X. Li, S. Yang, W. Luo, Y. Zhang, S. Kim, D. Kim, S. Shinde, Y. Li, Z. Liu, Z. Jiang, J. Lee, In-situ reconstructed Ru atom array on α-MnO_2 with enhanced performance for acidic water oxidation, Nat. Catal. 4 (2021) 1012–1023.
[5] L. Zhang, Q. Wang, L. Li, M.N. Banis, J. Li, K. Adair, Y. Sun, R. Li, Z.-J. Zhao, M. Gu, X. Sun, Single atom surface engineering: a new strategy to boost electrochemical activities of Pt catalysts, Nano Energy 93 (2022) 106813.
[6] Q. Dai, L. Wang, K. Wang, X. Sang, Z. Li, B. Yang, J. Chen, L. Lei, L. Dai, Y. Hou, Accelerated water dissociation kinetics by electron-enriched cobalt sites for efficient alkaline hydrogen evolution, Adv. Funct. Mater. (2021) 2109556.
[7] C. Jiang, J. Yang, X. Han, H. Qi, M. Su, D. Zhao, L. Kang, X. Liu, J. Ye, J. Li, Z.-X. Guo, N. Kaltsoyannis, A. Wang, J. Tang, Crystallinity-modulated $Co_{2-x}V_xO_4$ nanoplates for efficient electrochemical water oxidation, ACS Catal. 11 (2021) 14884–14891.
[8] H. Huang, H. Jung, S. Li, S. Kim, J.W. Han, J. Lee, Activation of inert copper for significantly enhanced hydrogen evolution behaviors by trace ruthenium doping, Nano Energy 92 (2022) 106763.
[9] L. Qi, Z. Zheng, C. Xing, Z. Wang, X. Luan, Y. Xue, F. He, Y. Li, 1D nanowire heterojunction electrocatalysts of $MnCo_2O_4$/GDY for efficient overall water splitting, Adv. Funct. Mater. (2021) 2107179.
[10] Y. Chang, P. Zhai, J. Hou, J. Zhao, J. Gao, Excellent HER and OER catalyzing performance of Se-vacancies in defects-engineered $PtSe_2$: from simulation to experiment, Adv. Energy Mater. (2021) 2102359.
[11] Y. Ge, X. Wang, B. Chen, Z. Huang, Z. Shi, B. Huang, J. Liu, G. Wang, Y. Chen, L. Li, S. Lu, Q. Luo, Q. Yun, H. Zhang, Preparation of fcc-2H-fcc heterophase Pd@Ir nanostructures for high-performance electrochemical hydrogen evolution, Adv. Mater. (2021) 2107399.
[12] X. Tong, Y. Zhao, Z. Zhuo, Z. Yang, S. Wang, Y. Liu, N. Lu, H. Li, T. Zhai, Dual-regulation of defect sites and vertical conduction by spiral domain for electrocatalytic hydrogen, Evol., Angew. Chem. Int. Ed. (2021) 2112953.
[13] S. Ibraheem, G. Yasin, A. Kumar, M.A. Mushtaq, S. Ibrahim, R. Iqbal, M. Tabish, S. Ali, A. Saad, Appl. Iron-cation-coordinated cobalt-bridged-selenides nanorods for highly efficient photo/electrochemical water splitting, Catal. B: Environ. 304 (2022) 120987.
[14] G. Qian, J. Chen, T. Yu, L. Luo, S. Yin, N-doped graphene-decorated NiCo alloy coupled with mesoporous NiCoMoO nano-sheet heterojunction for enhanced water electrolysis activity at high current density, Nano Micro Lett. 13 (2021) 77.
[15] S. Ye, Y. Lei, T. Xu, L. Zheng, Z. Chen, X. Yang, X. Ren, Y. Li, Q. Zhang, J. Liu, Deeply self-reconstructing CoFe(H3O)(PO4)2 to low-crystalline Fe0.5Co0.5OOH with Fe3+-O-Fe3+ motifs for oxygen evolution reaction, Appl. Catal. B Environ. 304 (2022) 120986.
[16] T. Xiong, X. Yao, Z. Zhu, R. Xiao, Y.W. Hu, Y. Huang, S. Zhang, M.J.T. Balogun, In situ grown Co-based interstitial compounds: non-3d metal and non-metal dual modulation boosts alkaline and acidic hydrogen electrocatalysis, Small (2021) 2105331.
[17] S. Chen, S. Wang, P. Hao, M. Li, Y. Zhang, J. Guo, W. Ding, M. Liu, J. Wang, X. Guo, N.,O.-C. Nanocage-mediated, high-efficient hydrogen evolution reaction on IrNi@N,O-C electrocatalyst, Appl. Catal. B Environ. 304 (2022) 120996.
[18] G. Di Liberto, L.A. Cipriano, G. Pacchioni, Role of dihydride and dihydrogen complexes in hydrogen evolution reaction on single-atom catalysts, J. Am. Chem. Soc. 143 (2021) 20431–20441.
[19] X. Tong, Y. Li, N. Pang, Y. Qu, C. Yan, D. Xiong, S. Xu, L. Wang, P.K. Chu, Co-doped Ni_3S_2 porous nanocones as high-performance bifunctional electrocatalysts in water splitting, Chem. Eng. J. 425 (2021) 130455.
[20] T. Liang, A. Wang, D. Ma, Z. Mao, J. Wang, J. Xie, Low-dimensional transition metal sulfide-based electrocatalysts for water electrolysis: overview and perspectives, Nanoscale 14 (2022) 17841–17861.
[21] X. Tong, N. Pang, Y. Qu, C. Yan, D. Xiong, S. Xu, L. Wang, P.K. Chu, 3D urchin-like NiCo2O4 coated with carbon nanospheres prepared on flexible graphite felt for efficient bifunctional electrocatalytic water splitting, J. Mater. Sci. 56 (2021) 9961–9973.
[22] L. Huang, Z. Li, S. Sun, G. Sun, Y. Li, S. Han, J. Lian, NiS/MoS2 complex grown on carbon paper as a bifunctional electrocatalyst for full water splitting, J. Alloys Compd 926 (2022) 166870.
[23] A.P. Tiwari, K. Kim, S. Jeon, Improving intrinsic electrocatalytic activity of layered transition metal chalcogenides as electrocatalysts for water splitting, Curr. Opin. Electrochem 34 (2022) 100982.
[24] S. Geng, F. Tian, M. Li, Y. Liu, J. Sheng, W. Yang, Y. Yu, Y. Hou, Activating interfacial S sites of MoS_2 boosts hydrogen evolution electrocatalysis, Nano Res. 15 (2021) 1809–1816.
[25] K. Cao, S. Sun, A. Song, J. Ba, H. Lin, X. Yu, C. Xu, B. Jin, J. Huang, D. Fan, Increased 1T-MoS_2 in MoS_2 @CoS_2/G composite for high-efficiency hydrogen evolution reaction, J. Alloy. Compd. 907 (2022) 164539.

[26] B. Wang, H. Huang, M. Huang, P. Yan, T.T. Isimjan, X. Yang, Electron-transfer enhanced MoO_2-Ni heterostructures as a highly efficient pH-universal catalyst for hydrogen evolution, Sci. China Chem. 63 (2020) 841–849.

[27] Q. Wang, Y. Lei, Y. Wang, Y. Liu, C. Song, J. Zeng, Y. Song, X. Duan, D. Wang, Y. Li, Atomic-scale engineering of chemical-vapor-deposition-grown 2D transition metal dichalcogenides for electrocatalysis, Energy Environ. Sci. 13 (2020) 1593–1616.

[28] Z. Zheng, L. Yu, M. Gao, X. Chen, W. Zhou, C. Ma, L. Wu, J. Zhu, X. Meng, J. Hu, Y. Tu, S. Wu, J. Mao, Z. Tian, D. Deng, Boosting hydrogen evolution on MoS_2 via co-confining selenium in surface and cobalt in inner layer, Nat. Commun. 11 (2020) 3315.

[29] X. Hou, H. Zhou, M. Zhao, Y. Cai, Q. Wei, MoS_2 nanoplates embedded in Co–N-doped carbon nanocages as efficient catalyst for HER and OER, ACS Sustain. Chem. Eng. 8 (2020) 5724–5733.

[30] Y.C. Ruan, Y.M. Xie, X.L. Chen, L. Dong, F.F. Zhang, T.T. Yang, X.F. Luo, M.Y. Cheng, P.F. Yin, C.K. Dong, K. Lin, D.J. Li, H. Liu, X.W. Du, Exposing Cu(100) surface via ion-implantation-induced oxidization and etching for promoting hydrogen evolution reaction, Langmuir 38 (2022) 2993–2999.

[31] N. Wei, S. Zhang, X. Yao, X. Hu, Z. Sun, V. Nica, J. Yang, Q. Zhou, Structural and electronic engineering of zirconium-induced bimetallic phosphides supported by nitrogen-doped carbon fibers for highly efficient oxygen evolution reaction, Int. J. Hydrog. Energy 47 (2022) 35254–35264.

[32] X. Tong, Y. Li, Q. Ruan, N. Pang, Y. Zhou, D. Wu, D. Xiong, S. Xu, L. Wang, P.K. Chu, Plasma engineering of basal sulfur sites on MoS2@Ni3S2 nanorods for the alkaline hydrogen evolution reaction, Adv. Sci. (2021) 210477.

[33] Y. Zhou, X. Tong, N. Pang, Y. Deng, C. Yan, D. Wu, S. Xu, D. Xiong, L. Wang, P.K. Chu, Ni_3S_2 nanocomposite structures doped with Zn and Co as long-lifetime, high-energy-density, and binder-free cathodes in flexible aqueous nickel-zinc batteries, ACS Appl. Mater. Interfaces 13 (2021) 34292–34300.

[34] G. Kresse, J. Furthmüller, Efficient iterative schemes for ab initio total-energy calculations using a plane-wave basis set, Phys. Rev. B 54 (1996) 11169.

[35] J.P. Perdew, K. Burke, M. Ernzerhof, Generalized gradient approximation made simple, Phys. Rev. Lett. 77 (1996) 3865.

[36] P.E. Blöchl, Projector augmented-wave method, Phys. Rev. B 50 (1994) 17953.

[37] S.L. Dudarev, G.A. Botton, S.Y. Savrasov, C.J. Humphreys, A.P. Sutton, Electron-energy-loss spectra and the structural stability of nickel oxide: An LSDA+U study, Phys. Rev. B 57 (1998) 1505.

[38] H. Xu, Y. Jiao, S. Li, H. Meng, J. Wu, X. Shi, Z. Du, R. Wang, G. Tian, Ultrathin-layered MoS_2 hollow nanospheres decorating Ni_3S_2 nanowires as high effective self-supporting electrode for hydrogen evolution reaction, Int. J. Hydrog. Energy 45 (2020) 13149–13162.

[39] F. Lin, R. Tian, P. Dong, G. Jiang, F. He, S. Wang, R. Fu, C. Zhao, Y.Y. Gu, S. Wang, Defect-rich MoS_2/NiS_2 nanosheets loaded on SiNWs for efficient and stable photoelectrochemical hydrogen production, J. Colloid Interface Sci. 631 (2023) 133–142.

[40] J. Zhang, T. Wang, D. Pohl, B. Rellinghaus, R. Dong, S. Liu, X. Zhuang, X. Feng, Interface engineering of MoS_2 /Ni_3S_2 heterostructures for highly enhanced electrochemical overall-water-splitting activity, Angew. Chem. Int. Ed. Engl. 55 (2016) 6702–6707.

[41] X. Tong, Y. Li, N. Pang, Y. Zhou, D. Wu, D. Xiong, S. Xu, L. Wang, P.K. Chu, Highly active cobalt-doped nickel sulfide porous nanocones for high-performance quasi-solid-state zinc-ion batteries, J. Energy Chem. 66 (2022) 237–249.

[42] D.C. Nguyen, T.L. Luyen Doan, S. Prabhakaran, D.T. Tran, D.H. Kim, J.H. Lee, N.H. Kim, Hierarchical Co and Nb dual-doped MoS_2 nanosheets shelled micro-TiO_2 hollow spheres as effective multifunctional electrocatalysts for HER, OER, and ORR, Nano Energy 82 (2021) 105750.

[43] Y. Deng, X. Tong, N. Pang, Y. Zhou, D. Wu, S. Xu, D. Xiong, L. Wang, P.K. Chu, 3D MoS_2/Ni_3S_2 heterogeneous nanorod arrays as high-performance cathode for quasi-solid-state alkaline zinc batteries, Appl. Surf. Sci. 572 (2022) 151442.

[44] B. Pattengale, Y. Huang, X. Yan, S. Yang, S. Younan, W. Hu, Z. Li, S. Lee, X. Pan, J. Gu, J. Huang, Dynamic evolution and reversibility of single-atom Ni (II) active site in 1 T-MoS_2 electrocatalysts for hydrogen evolution, Nat. Commun. 11 (2020) 4114.

[45] J.S. Lee, R. Saroha, S.H. Oh, D.H. Shin, S.M. Jeong, J.K. Kim, J.S. Cho, Rational design of perforated bimetallic (Ni, Mo) sulfides/N-doped graphitic carbon composite microspheres as anode materials for superior Na-ion batteries, Small Methods 5 (2021) 2100195.

[46] J. Kibsgaard, Z. Chen, B.N. Reinecke, T.F. Jaramillo, Engineering the surface structure of MoS_2 to preferentially expose active edge sites for electrocatalysis, Nat. Mater. 11 (2012) 963–969.

[47] Y. Zhang, H. Guo, M. Song, Z. Qiu, S. Wang, L. Sun, Hierarchical interfaces engineering-driven of the CoS_2/MoS_2/Ni_3S_2/NF electrode for high-efficient and stable oxygen evolution and urea oxidation reactions, Appl. Surf. Sci. 617 (2023).

[48] H. Li, S. Yin, G. Dong, G. Cui, C. Lei, Y. Li, X. Xu, L. Feng, J. Zhang, C. Yu, Effect of humidity on optical and electrical properties of Zr-doped In_2O_3 and a new structure for transparent electrode of silicon heterojunction solar cell, Sol. Energy 196 (2020) 125–131.

[49] D.N. Sangeetha, M.S. Santosh, M. Selvakumar, Flower-like carbon doped MoS2/Activated carbon composite electrode for superior performance of supercapacitors and hydrogen evolution reactions, J. Alloy. Compd. 831 (2020) 154745.

[50] M. Cong, D. Sun, L. Zhang, X. Ding, In situ assembly of metal-organic framework-derived N-doped carbon/Co/CoP catalysts on carbon paper for water splitting in alkaline electrolytes, Chin. J. Catal. 41 (2020) 242–248.

[51] T. Ouyang, Y.Q. Ye, C.Y. Wu, K. Xiao, Z.Q. Liu, Heterostructures Composed of N-Doped Carbon Nanotubes Encapsulating Cobalt and beta-Mo2C Nanoparticles as Bifunctional Electrodes for Water Splitting, Angew. Chem. Int. Ed. Engl. 58 (2019) 4923–4928.

[52] Z. Fu, Z. Jiang, T. Hu, Z.J. Jiang, Hierarchical nanoassembly of Ni/MoS_2@$Ni_{12}P_5$/ZnP_2 achieved by a plasma assisted phosphorization with highly improved electrocatalytic activity for overall water splitting, Electrochim. Acta 419 (2022) 140392.

[53] X. Ji, Y. Lin, J. Zeng, Z. Ren, Z. Lin, Y. Mu, Y. Qiu, J. Yu, Graphene/MoS_2/FeCoNi$(OH)_x$ and Graphene/MoS_2/FeCoNiP_x multilayer-stacked vertical nanosheets on carbon fibers for highly efficient overall water splitting, Nat. Commun. 12 (2021) 1380.

[54] X.P. Li, L.R. Zheng, S.J. Liu, T. Ouyang, S. Ye, Z.Q. Liu, Heterostructures of NiFe LDH hierarchically assembled on MoS_2 nanosheets as high-efficiency electrocatalysts for overall water splitting, Chin. Chem. Lett. 33 (2022) 4761–4765.

[55] X. Luo, P. Ji, P. Wang, R. Cheng, D. Chen, C. Lin, J. Zhang, J. He, Z. Shi, N. Li, S. Xiao, S. Mu, Interface engineering of hierarchical branched Mo-doped Ni_3S_2/Ni_xP_y hollow heterostructure nanorods for efficient overall water splitting, Adv. Energy Mater. 10 (2020) 1903891.

[56] Y.K. Li, G. Zhang, W.T. Lu, F.F. Cao, Amorphous Ni-Fe-Mo suboxides coupled with ni network as porous nanoplate array on nickel foam: a highly efficient and durable bifunctional electrode for overall water splitting, Adv. Sci. 7 (2020) 1902034.

[57] G.L. Li, Y.Y. Miao, X.Y. Qiao, T.-Y. Wang, F. Deng, Engineering edge sites based on NiS_2/MoS_2/CNTs heterojunction catalyst for overall water splitting, Appl. Surf. Sci. 615 (2023) 156309.

[58] B. Fei, Z. Chen, J. Liu, H. Xu, X. Yan, H. Qing, M. Chen, R. Wu, Ultrathinning nickel sulfide with modulated electron density for efficient water splitting, Adv. Energy Mater. 10 (2020) 2001963.

[59] L. Guo, Q. Liu, Y. Liu, Z. Chen, Y. Jiang, H. Jin, T. Zhou, J. Yang, Y. Liu, Self-supported tremella-like MoS_2-AB particles on nickel foam as bifunctional electrocatalysts for overall water splitting, Nano Energy 92 (2022) 106707.

[60] Y. Li, C. Wang, M. Cui, J. Xiong, L. Mi, S. Chen, Heterostructured MoO_2@MoS_2@Co_9S_8 nanorods as high efficiency bifunctional electrocatalyst for overall water splitting, Appl. Surf. Sci. 543 (2021) 148804.

[61] H. Liu, D. Ouyang, Q. Zhou, C. Feng, Successional heterostructure MoS_2-Ni_3S_2 nanospheres based on 3D nano-porous Ni: an efficient electrocatalyst for overall water splitting, J. Alloy. Compd. 920 (2022) 165243.

[62] C. Wang, X. Shao, J. Pan, J. Hu, X. Xu, Redox bifunctional activities with optical gain of Ni_3S_2 nanosheets edged with MoS_2 for overall water splitting, Appl. Catal. B: Environ. 268 (2020) 118435.

[63] M. Kim, H. Seok, N. Clament Sagaya Selvam, J. Cho, G.H. Choi, M.G. Nam, S. Kang, T. Kim, P.J. Yoo, Kirkendall effect induced bifunctional hybrid electrocatalyst (Co_9S_8@MoS_2/N-doped hollow carbon) for high performance overall water splitting, J. Power Sources 493 (2021) 229688.

[64] L. Wang, X. Duan, X. Liu, J. Gu, R. Si, Y. Qiu, Y. Qiu, D. Shi, F. Chen, X. Sun, J. Lin, J. Sun, Atomically dispersed Mo supported on metallic Co_9S_8 nanoflakes as an advanced noble-metal-free bifunctional water splitting catalyst working in universal pH conditions, Adv. Energy Mater. 10 (2019) 1903137.

[65] G. Zhou, X. Wu, M. Zhao, H. Pang, L. Xu, J. Yang, Y. Tang, Interfacial engineering-triggered bifunctionality of CoS_2 /MoS_2 nanocubes/nanosheet arrays for high-efficiency overall water splitting, ChemSusChem 14 (2021) 699–708.

[66] M.Y. Toriyama, A.M. Ganose, M. Dylla, S. Anand, J. Park, M.K. Brod, J.M. Munro, K.A. Persson, A. Jain, G.J. Snyder, How to analyse a density of states, Mater. Today Electron. 1 (2022) 100002.

Supporting Information

Activation of basal-plane sulfur sites on MoS_2@Ni_3S_2 nanorods by Zr plasma ion implantation for bifunctional electrocatalysts

Ning Pang[a 1], Yun Li[c 1], Xin Tong[a, b, e], Mengqiu Wang[a], Huiyun Shi[a], Dajun Wu[b], Dayuan Xiong[a], Shaohui Xu[a], Lianwei Wang[a, e*],Lin Jiang[d*], Paul K. Chu[e]

[a] *Key Laboratory of Polar Materials and Devices (MOE), Department of Electronics, East China Normal University, Shanghai 200241, China*

[b] *Jiangsu Laboratory of Advanced Functional Materials, School of Electronic and Information Engineering, Changshu Institute of Technology, Changshu 215500, China*

[c] *School of Physics and Electronic Engineering, Hanshan Normal University, Chaozhou 521041, China*

[d] *School of Microelectronics, Shanghai University, 20 Chengzhong Road, Shanghai 201800, China*

[e] *Department of Physics, Department of Materials Science and Engineering, and Department of Biomedical Engineering, City University of Hong Kong, Kowloon, Hong Kong, China*

First-principles calculation

According to previous reports, the key steps in HER in an alkaline environment are as follows:

S1: $S + H_2O + e^- \rightarrow S - H^* + OH^-$ $(Volmer\ step)$

S2: $S - H^* + H_2O + e^- \rightarrow S + OH^- + H^2\uparrow$ $(Heyrovsky\ step)$

S3: $2(S - H^*) \rightarrow 2S + H^2\uparrow$ $(Tafel\ step)$

In the last part of hydrogen production, H^* is expressed as an intermediate state and the details of the reaction process of the Tafel and Heyrovsky steps are different, but according to the zero point of the H_2 desorption state, the calculation process of free energy is the same. The Gibbs free energy change can be expressed as:

S4: $\Delta G_{H*} = E(S - H^*) - E(S) - 1/2E(H_2) + \Delta(ZPE - T\Delta S)$,

where S represents S active sites at which HER occurs on the MoS_2 surface, E(S-H^*) and E(S)+1/2E(H_2) are the free energy before and after the reaction, respectively, and Δ(ZPE–TΔS) is the entropy thermal change.

Similarly, OER involves multiple proton-transfer processes as shown in **S5-S9**:

S5: $S + OH^- \rightarrow SOH^* + e^-$

S6: $SOH^* + OH^- \rightarrow SO^* + H_2O + e^-$

S7: $SO^* + OH^- \rightarrow SOOH^* + e^-$

S8: $SOOH^* + OH^- \rightarrow SOO^* + H_2O + e^-$

S9: $SOO^* \rightarrow S + O_2$.

Here, S also represents the active site when OER occurs and SOH^*, SO^*, $SOOH^*$ are the intermediate species adsorbed on the active sites. In order to evaluate the OER activity, the free energy ($\Delta G_1 \sim \Delta G_4$) is computed based on the computational standard hydrogen electrode model. The free energy can be obtained as follows:

S10: $\Delta G_1 = E(MOH^*) - E(M) - E(H2O) + 1/2E(H_2) - eU + \Delta G_{H+}(pH) + \Delta(ZPE - T\Delta S)$

S11: $\Delta G_2 = E(MO^*) - E(MOH^*) - E(H2O) + 1/2E(H_2) - eU + \Delta G_{H+}(pH) + \Delta(ZPE - T\Delta S)$

S12: $\Delta G_3 = E(MOOH^*) - E(MO^*) - E(H2O) + 1/2E(H_2) - eU + \Delta G_{H+}(pH) + \Delta(ZPE - T\Delta S)$

S13: $\Delta G_{4,5} = 4 \times 1.23 - \Delta G_1 - \Delta G_2 - \Delta G_3$

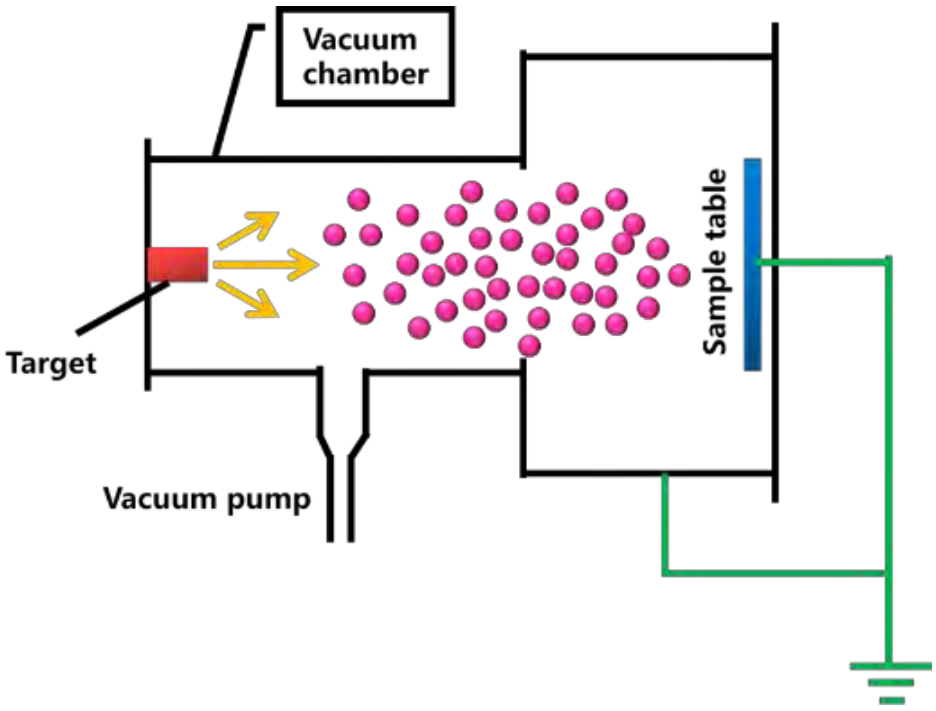

Fig. S1. High energy metal plasma injection system.

(a)

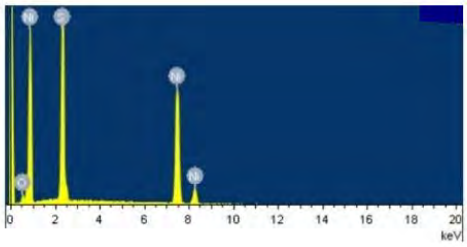

(b)

Element	Wt%	At%
O K	3.40	9.52
S K	26.65	37.18
Ni K	69.95	53.31
Total	100.00	

Fig. S2. (a) EDS spectrum of Ni_3S_2/NF and (b) Elemental concentrations.

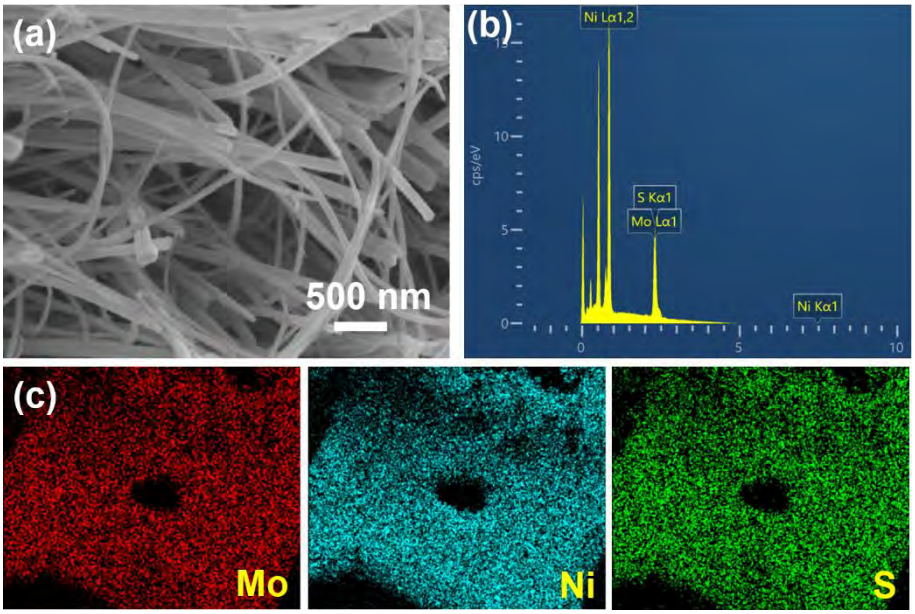

Fig. S3. (a) SEM image of MSNF, (b) EDS spectrum of MSNF, and (c) EDS elemental maps of Mo, Ni, and S.

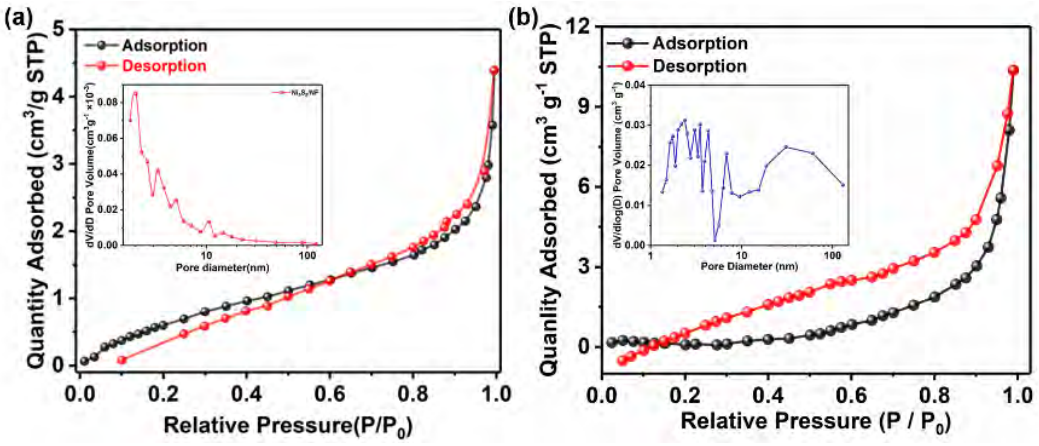

Fig. S4. N_2 adsorption/desorption isotherms and pore size distribution (inset): (a) Ni_3S_2/NF and (b) MSNF.

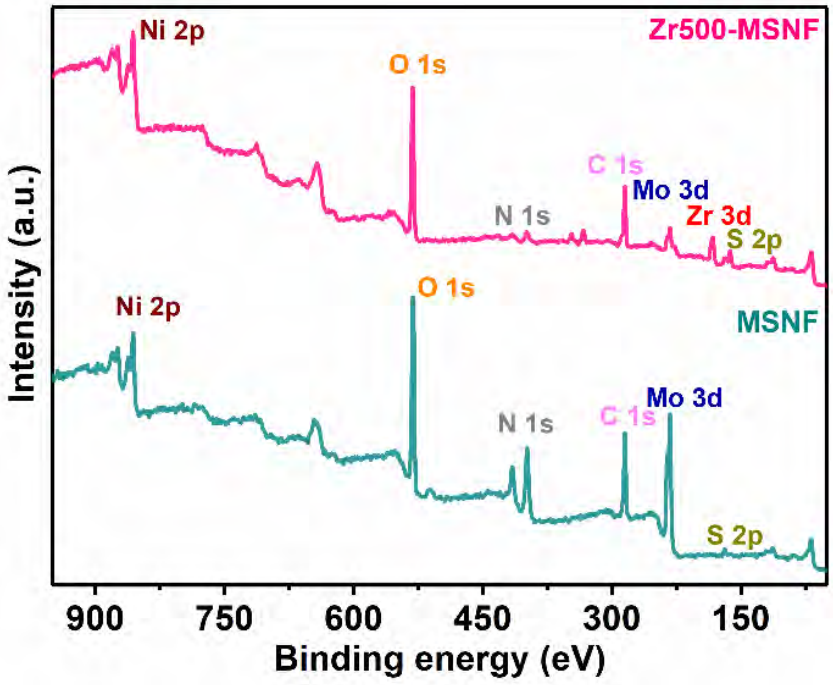

Fig. S5. XPS survey spectrum of MSNF and Zr500-MSNF.

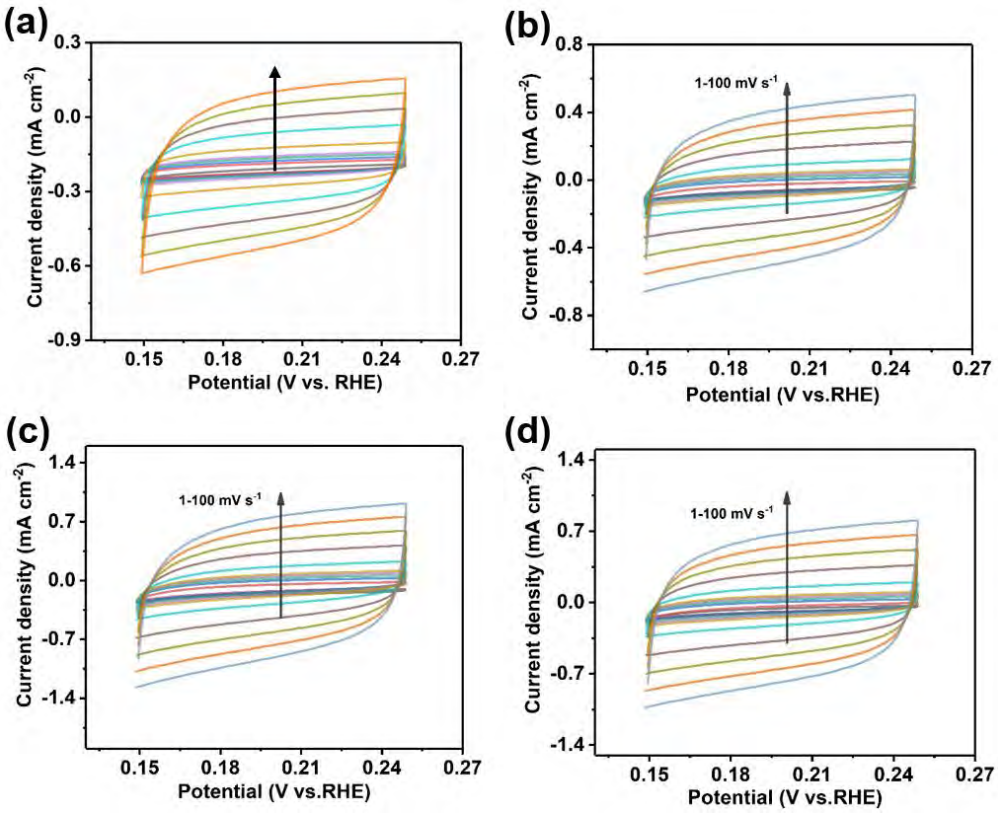

Fig. S6. CV acquired at different scanning rates in the non-Faraday region.

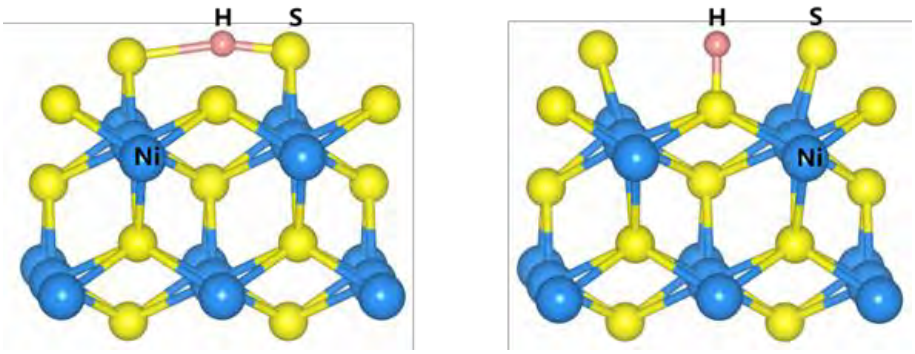

Fig. S7. 3D model showing H* adsorption on different S sites on Ni_3S_2 (110).

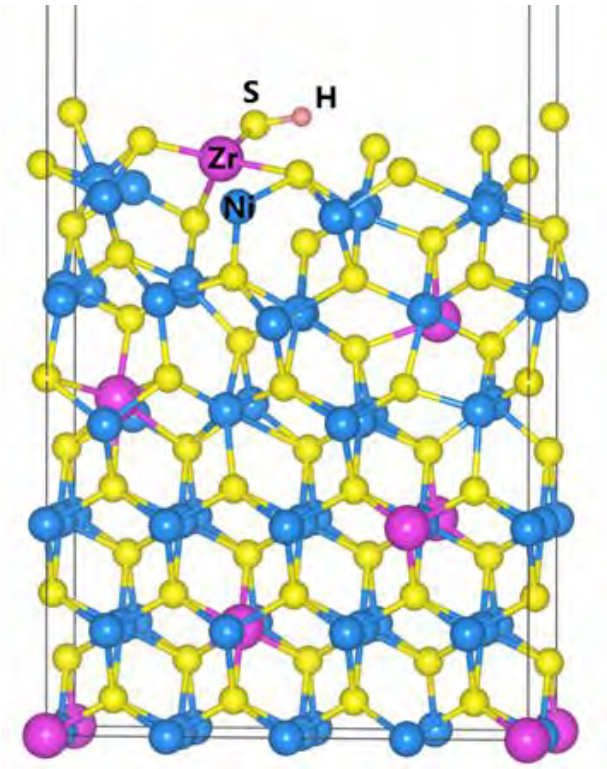

Fig. S8. Model showing H* adsorption on the Zr-doped Ni_3S_2 (110) surface.

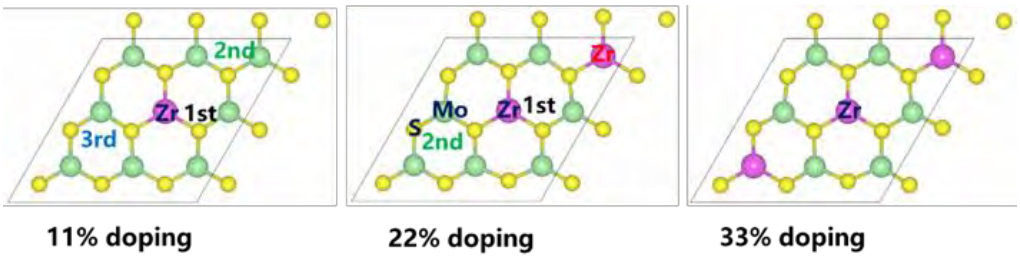

Fig. S9. Top view of the Zr-doped MoS_2 models for different concentrations.

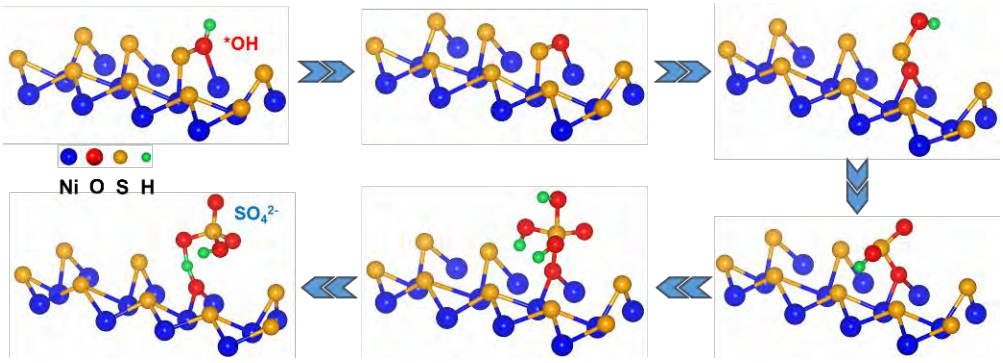

Fig. S10. Schematic illustration of nickel sulfide adsorbing hydroxide radicals and being oxidized to form nickel hydroxide and sulfate radicals.

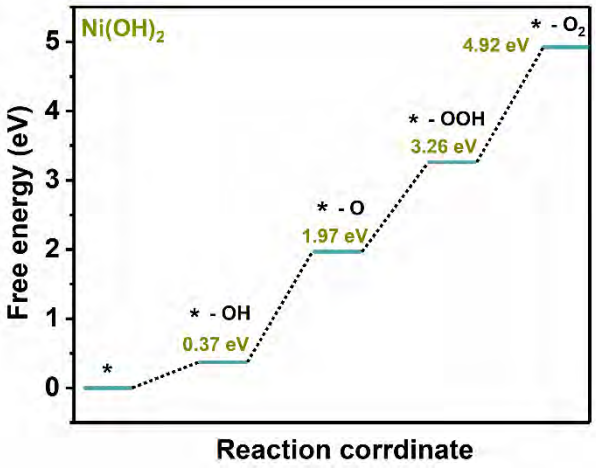

Fig. S11. Free energy diagram of $Ni(OH)_2$ in OER.

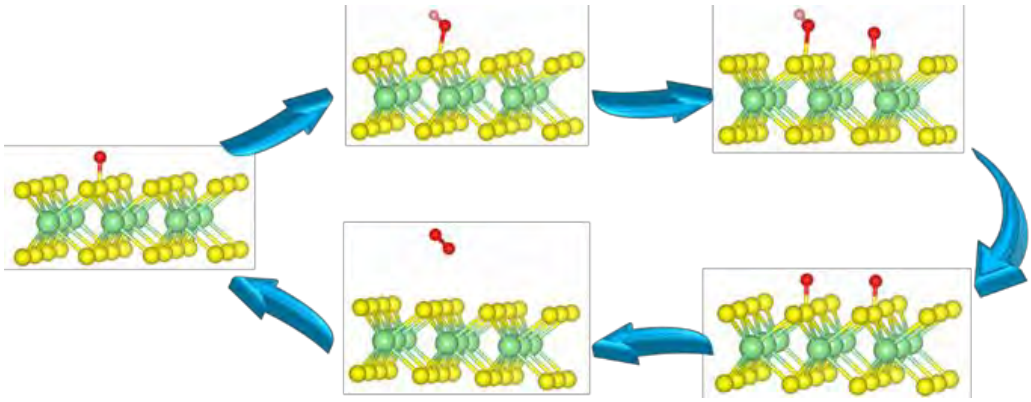

Fig. S12. Schematic diagram of the oxygen evolution process on the surface of MoS_2.

Fig. S13. Photograph of the overall water splitting device.

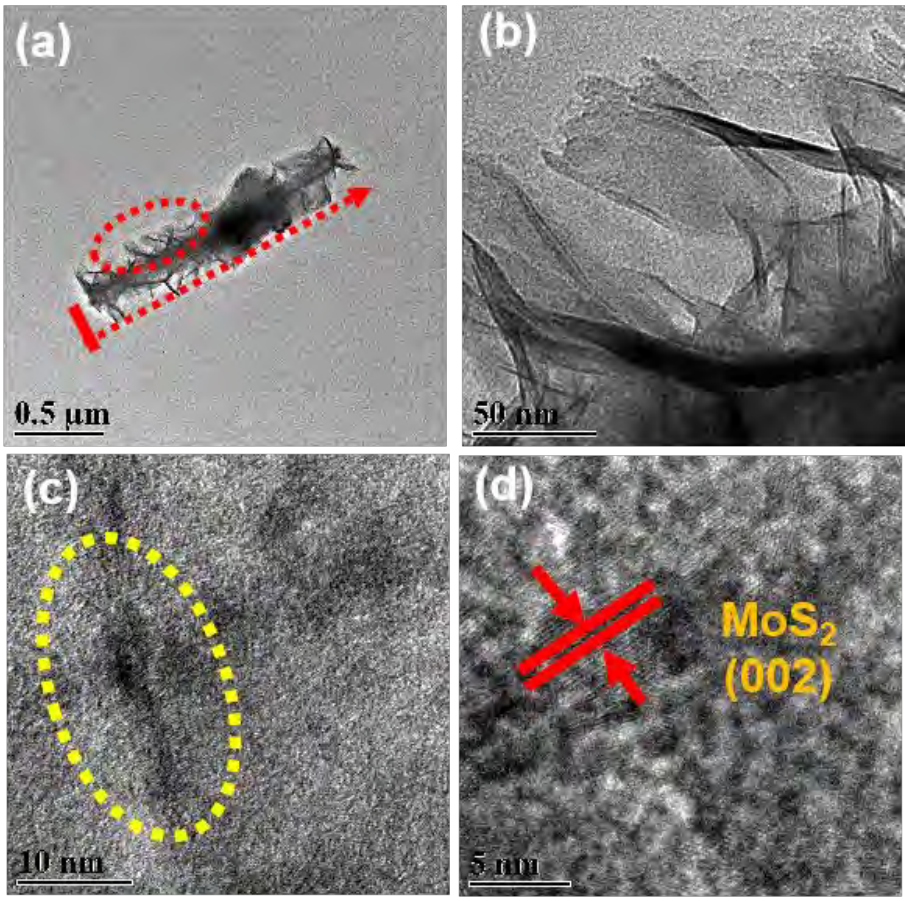

Fig. S14. TEM and HR-TEM images of Zr500-MSNF after the stability test.

References

[S1] X. Tong, Y. Li, N. Pang, Y. Qu, C. Yan, D. Xiong, S. Xu, L. Wang, P.K. Chu, Co-doped Ni_3S_2 porous nanocones as high-performance bifunctional electrocatalysts in water splitting, Chem. Eng. J. 425 (2021) 130455.

[S2] C. Hu, L. Zhang, J. Gong, Recent progress made in the mechanism comprehension and design of electrocatalysts for alkaline water splitting, Energy Environ. Sci. 12 (2019) 2620-2645.

[S3] D. Kong, H. Wang, Z. Lu, Y. Cui, $CoSe_2$ Nanoparticles Grown on Carbon Fiber Paper: An Efficient and Stable Electrocatalyst for Hydrogen Evolution Reaction, J. Am. Chem. Soc. 136 (2014) 4897-4900.

[S4] Q. Wang, Y. Lei, Y. Wang, Y. Liu, C. Song, J. Zeng, Y. Song, X. Duan, D. Wang, Y. Li, Atomic-scale engineering of chemical-vapor-deposition-grown 2D transition metal dichalcogenides for electrocatalysis, Energy Environ. Sci. 13 (2020) 1593-1616.

[S5] Y. Yang, Y. Qian, H. Li, Z. Zhang, Y. Mu, D. Do, B. Zhou, J. Dong, W. Yan, Y. Qin, L. Fang, R. Feng, J. Zhou, P. Zhang, J. Dong, G. Yu, Y. Liu, X. Zhang, X. Fan, O-coordinated W-Mo dual-atom catalyst for pH-universal electrocatalytic hydrogen evolution, Sci. Adv. 6 (2020) 6586.

[S6] Z. Zheng, L. Yu, M. Gao, X. Chen, W. Zhou, C. Ma, L. Wu, J. Zhu, X. Meng, J. Hu, Y. Tu, S. Wu, J. Mao, Z. Tian, D. Deng, Boosting hydrogen evolution on MoS_2 via co-confining selenium in surface and cobalt in inner layer, Nat. Commun. 11 (2020) 3315.

[S7] Y. Liu, S. Jiang, S. Li, L. Zhou, Z. Li, J. Li, M. Shao, Interface engineering of (Ni,

Fe)S_2@MoS_2 heterostructures for synergetic electrochemical water splitting, Appl. Catal. B: Environ. 247 (2019) 107-114.

[S8] H. Zhang, D.J. Hagen, X. Li, A. Graff, F. Heyroth, B. Fuhrmann, I. Kostanovskiy, S.L. Schweizer, F. Caddeo, A.W. Maijenburg, S. Parkin, R.B. Wehrspohn, Atomic Layer Deposition of Cobalt Phosphide for Efficient Water Splitting, Angew. Chem. Int. Ed. 59 (2020) 17172-17176.

[S9] X. Tong, Y. Li, Q. Ruan, N. Pang, Y. Zhou, D. Wu, D. Xiong, S. Xu, L. Wang, P.K. Chu, Plasma Engineering of Basal Sulfur Sites on MoS_2@Ni_3S_2 Nanorods for the Alkaline Hydrogen Evolution Reaction, Adv. Sci. (2021) 2104774.

[S10] Y. Li, H. Wang, L. Xie, Y. Liang, G. Hong, H. Dai, MoS_2 Nanoparticles Grown on Graphene: An Advanced Catalyst for the Hydrogen Evolution Reaction, J. Am. Chem. Soc. 133 (2011) 7296-7299.

[S11] Z. Chen, D. Cummins, B.N. Reinecke, E. Clark, M.K. Sunkara, T.F. Jaramillo, Core-shell MoO_3-MoS_2 Nanowires for Hydrogen Evolution: A Functional Design for Electrocatalytic Materials, Nano Lett. 11 (2011) 4168-4175.

[S12] B. Pattengale, Y. Huang, X. Yan, S. Yang, S. Younan, W. Hu, Z. Li, S. Lee, X. Pan, J. Gu, J. Huang, Dynamic evolution and reversibility of single-atom Ni (II) active site in 1 T-MoS_2 electrocatalysts for hydrogen evolution, Nat. Commun. 11 (2020) 4114.

[S13] J. Kibsgaard, Z. Chen, B.N. Reinecke, T.F. Jaramillo, Engineering the surface structure of MoS_2 to preferentially expose active edge sites for electrocatalysis, Nat. Mater. 11 (2012) 963-969.